Methane and nitrous oxide concentrations and sea-air fluxes in western Long Island Sound, a eutrophic urban estuary: Hourly to seasonal variability

Cara C. M. Manning[1], Anagha Payyambally[1], Josie L. Mottram[1], and Kelsey Ward[1]

[1]University of Connecticut, Department of Marine Sciences, Groton, CT, 06340, USA

Correspondence to: Cara C. M. Manning (cara.manning@uconn.edu)

This manuscript is a preprint that has been submitted to *Elementa: Science of the Anthropocene*. It has been submitted to *EarthArXiv* to ensure rapid and free access to the work. This version of the manuscript has been revised based on one round of peer reviewer feedback. The manuscript has not yet been accepted for publication. Subsequent versions may contain different content.

If accepted in a peer-reviewed journal, the final manuscript will be available through the “peer-reviewed publication DOI” link on the *EarthArXiv* website.

Please contact the corresponding author if you have any questions or feedback about the manuscript.

Prior to publication in a peer-reviewed journal, please cite this manuscript as:
Manning, C.C.M., A. Payyambally, J.L. Mottram, and K. Ward (2026). Methane and nitrous oxide concentrations and sea-air fluxes in western Long Island Sound, a eutrophic urban estuary: Hourly to seasonal variability, *EarthArXiv*. https://doi.org/10.31223/X54T8Z

Methane and nitrous oxide concentrations and sea-air fluxes in western Long Island Sound, a eutrophic urban estuary: Hourly to seasonal variability

Cara C. M. Manning[1], Anagha Payyambally[1], Josie L. Mottram[1], and Kelsey Ward[1]

[1]University of Connecticut, Department of Marine Sciences, Groton, CT, 06340, USA

Correspondence to: Cara C. M. Manning (cara.manning@uconn.edu)

Abstract. Western Long Island Sound is a seasonally hypoxic urban estuary undergoing anthropogenic change, which may influence concentrations and emissions of the potent greenhouse gases methane (CH_4) and nitrous oxide (N_2O). To provide a benchmark of current gas distributions in this system, enabling detection of future changes and comparison with data from other estuaries worldwide, we obtained the first water column profiles of dissolved CH_4 and N_2O concentrations in western Long Island Sound. We collected samples at seven stations along an 18 km transect in August 2023, October 2023, and May 2024. CH_4 concentrations and sea-air fluxes were highest in August (mean concentration 101 nmol kg^{-1} and mean sea-air flux 154 μmol m^{-2} d^{-1}) and lowest in May (mean concentration 32 nmol kg^{-1} and mean sea-air flux 62 μmol m^{-2} d^{-1}). Conversely, N_2O concentrations and sea-air fluxes were highest in May (mean concentration 12.0 nmol kg^{-1} and mean sea-air flux 4.8 μmol m^{-2} d^{-1}) and lowest in August (mean concentration 10.1 nmol kg^{-1} and mean sea-air flux 2.5 μmol m^{-2} d^{-1}). Surface concentrations and sea-air fluxes of CH_4 and N_2O were highest at the westernmost station (closest to New York City) in all three seasons, suggesting that there is a persistent source of surface water to western Long Island Sound with high concentrations of CH_4 and N_2O. To investigate short-term variability in CH_4, N_2O, and oxygen (O_2), we collected samples every 4 hours over 28 hours at the middle station of the transect, in all three months. We concluded that there is measurable short-term variability in all three gases, and that the drivers of variability in these dissolved gases are complex and not dominated by tidal advection or light levels alone.

Keywords: methane; nitrous oxide; oxygen; hypoxia; estuary; diel cycle

1. Introduction

Long Island Sound (LIS) is an urban estuary that receives wastewater discharge from the most populous city in the USA, New York City, and undergoes seasonal hypoxia. Hypoxic conditions, often defined as dissolved oxygen (O_2) concentrations lower than 64 μmol L^{-1} (2 mg L^{-1}), can be harmful or fatal to a range of marine life (Diaz and Rosenberg, 2008; Vaquer-Sunyer and Duarte, 2008). Eutrophication (excess nitrogen inputs from human activities, including point source wastewater discharge and runoff) contributes to hypoxia in LIS by driving the overproduction of photosynthetic organisms at the surface and consumption of O_2 at depth from decomposition (Parker and O'Reilly, 1991; Varekamp et al., 2014).

Regionally, hypoxia is most severe in western LIS due to the restricted circulation and proximity to wastewater inputs from New York City (Lee and Lwiza, 2008; Whitney and Vlahos, 2021). The East River is a tidal estuary between Manhattan and Brooklyn/Queens which discharges Hudson River water and New York City wastewater into western LIS (Figure 1). There are currently six wastewater treatment plants in the East River which collectively discharge wastewater from 4 million of the 8 million residents of New York City (NYCDEP, 2025). These wastewater treatment plants contributed a nitrogen (N) loading of 2 x 10^6 kg N y^{-1} in 2016, accounting for >95% of the total N load from the East River, 18% of the total N loading to LIS in 2016 (Vaudrey, 2017), and 11% of the N load to LIS from 1995−2016 (Vlahos et al., 2020). The East River is the largest source of freshwater to western LIS, with a mean surface advective flux of 260 m^3 s^{-1} (Gay et al., 2004; Vlahos et al., 2020). The majority of the N load from larger rivers in the eastern and central LIS, such as the Connecticut River (mean discharge 500 m^3 s^{-1}), does not enter western LIS (Gay et al., 2004; Vlahos et al., 2020). For western LIS, Vlahos et al. (2020) determined that the East River is likely the largest source of N, contributing (3.2 ± 2.2) × 10^6 kg N y^{-1}, as compared to other rivers which contributed (2.6 ± 0.8) × 10^6 kg N y^{-1}, atmospheric deposition which contributed (1.2 ± 0.2) × 10^6 kg N y^{-1}, and lateral transport from central LIS which contributed (0.3 ± 1.7) × 10^6 kg N y^{-1} for the period 1995−2016. The study of Vlahos et al. (2020) defined western LIS to include all areas west of the Housatonic River; since our study focuses on only the westernmost half of this region, the influence of the East River will be even more prominent (Figure 1). Prior observations in the East River have demonstrated elevated nutrient levels associated with wastewater input in this system (Bowman, 1977; Li et al., 2018; Wallace, 2020). Wastewater treatment plant upgrades over recent decades have reduced the amount of N pollution entering LIS by 60% from the year 2000 baseline and reduced the 5-year average overall hypoxic area in LIS. However, hypoxia continues to occur annually in western LIS and the hypoxic area in the far western sound actually increased from 2017 to 2023 (Whitney and Vlahos, 2021; Duvall et al., 2024). Ongoing and future climate change contributes to the persistence of hypoxia in western LIS: warming temperatures reduce the solubility of O_2 in water and may also increase respiration rates and stratification (Parker and O'Reilly, 1991; Wilson et al., 2008; Irby et al., 2018; Whitney and Vlahos, 2021). Other temperate urban estuaries also experience interacting stressors from nutrient pollution and climate change (Howarth et al., 2011; Irby et al., 2018).

Methane (CH_4) and nitrous oxide (N_2O) are potent greenhouse gases that have a lower atmospheric concentration than carbon dioxide (CO_2), but much higher global warming potentials (heat trapping ability per unit mass) (Forster et al., 2021). Reported emissions of CH_4 and N_2O are widely variable across different coastal and estuarine systems (Robinson et al., 1998; Seitzinger et al., 2000; de Wilde and de Bie, 2000; Naqvi et al., 2010; Harley et al., 2015; Capelle and Tortell, 2016; Kock et al., 2016; Rosentreter et al., 2021; Zheng et al., 2022). For example, a recent global meta-analysis reported that published estuarine sea-air gas fluxes range from 0 to 50000 μmol m^{-2} d^{-1} for CH_4 and −60 to 500 μmol m^{-2} d^{-1} for N_2O (Zheng et al., 2022). Previous publications with data from LIS reported measurements of benthic N_2O and CH_4 production, groundwater-associated N_2O fluxes, and sedimentary CH_4 concentrations (Martens and Berner, 1974; Martens and Berner, 1977; Young et al., 2016; Mazur et al., 2021). To our knowledge there are no published water column measurements of N_2O or CH_4 concentrations or sea-air fluxes in LIS.

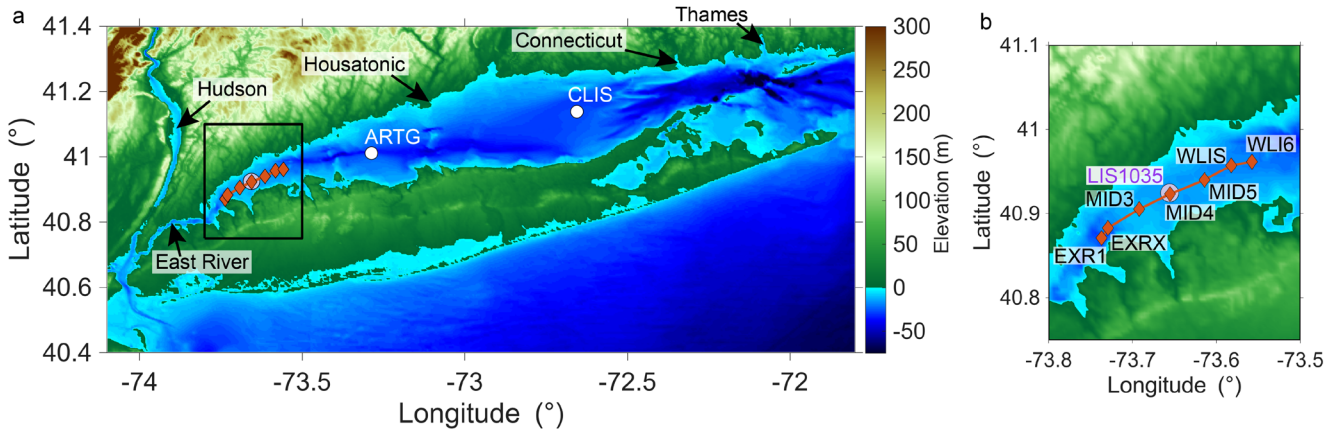

Figure 1. Maps of Long Island Sound and the transect sampled
The locations of stations sampled on each cruise are shown as orange diamonds and the stations sampled only in May 2024 (ARTG and CLIS) are shown with white circles (a). The station used for current speed predictions (LIS1035), near MID4, is shown with a purple circle. Large rivers influencing LIS are shown with black arrows (the Hudson, Housatonic, Connecticut, Thames, and East River). Elevation data was retrieved from The GEBCO Grid (GEBCO Compilation Group, 2024).
Alt Text: Map of the study area showing elevation above and below sea level and the locations of the stations at which data was collected. One panel shows all of LIS and the other shows the region near 40.9° N, 73.65° W where the water sampling transect was centered.

Biochemical reactions are associated with the production and consumption of CH_4 and N_2O (Reeburgh, 2007; Bange et al., 2010). CH_4 is produced and consumed through anaerobic and aerobic processes associated with organic matter diagenesis, chemotrophic reactions, the metabolism of methylated phosphorus and sulfur species, and photochemical reactions occurring in the water column, sediments, and sinking particles (Ward et al., 1987; Reeburgh, 2007; Mau et al., 2013; Damm et al., 2015; Repeta et al., 2016; Bianchi et al., 2018; Li et al., 2020; Fazi et al., 2021; Perez-Coronel and Beman, 2022; Hall et al., 2025). Anaerobic methanogenesis has previously been reported in LIS sediments in some of the earliest work on marine sedimentary organic matter diagenesis (Martens and Berner, 1974; Martens and Berner, 1977). The balance between these CH_4 sources and sinks influences estuarine emissions of CH_4 (Mao et al., 2022).

N_2O is generated as a byproduct during ammonium oxidation, the first step of nitrification, a chemoautotrophic process that yields energy from the conversion of ammonium to nitrite (NH_4^+ to NO_2^-) (Ward, 2008). Additionally, N_2O is an intermediate in heterotrophic denitrification, an anaerobic organic matter degradation process (Bange et al., 2010). Depending on environmental conditions, denitrification can either be a net source or sink of N_2O, with suboxic conditions tending to favor net N_2O production (incomplete denitrification) and anoxic conditions favoring N_2O consumption (complete denitrification) (Bange et al., 2010; Kock et al., 2016). Additionally, nitrification and denitrification can be coupled through the process of nitrifier denitrification, where the oxidation of NH_4^+ to NO_2^- is followed by reduction of NO_2^- to nitrogen gas (N_2) through intermediates, including N_2O (Wrage et al., 2001).

This study focused on CH_4 and N_2O dynamics in LIS. Our objectives were to obtain the first water column measurements of these gases, characterize hourly to seasonal variability, and calculate their sea-air fluxes. In coastal systems, biogeochemical parameters can vary on sub-daily timescales due to both physical and biological forcing (e.g., due to daily changes in tidal phase and light levels), but this variability has rarely been explored for CH_4 and N_2O. We evaluated how sampling time influences their concentrations and calculated fluxes. We determined the contribution of CH_4 and N_2O to the C and N budgets for LIS and compared their fluxes, after conversion to CO_2-equivalents, with previously published CO_2 data for western LIS. We place the results of this study in the context of other estuarine studies and discuss potential drivers of the observed trends. This study contributes new data to support broader scientific understanding of greenhouse gas dynamics in urban estuaries.

2. Methods

2.1 Sampling locations, timing, and procedures

We collected samples during cruises on the R/V *Connecticut* (2–3 August 2023, 19–20 October 2023, and 22–23 May 2024). On each cruise, we collected water column profiles at the same seven stations spanning an 18 km transect. These stations were sampled on day 2 over a 6-hour period, beginning at approximately 07:00 local time at the westernmost station (EXR1) and proceeding sequentially toward the easternmost station (WLI6). Two of the stations were sampled repeatedly: station MID4 was sampled every four hours over a 28-h period (eight times in total, beginning near 08:00 on day 1 and continuing until approximately 12:00 on day 2), and station EXRX was sampled at approximately 09:00 on days 1 and 2. For both EXRX and MID4, the final profile was collected as part of the seven-station transect on day 2. Station depths ranged from 13 to 32 m.

During the May 2024 cruise only, we sampled at stations CLIS and ARTG (closer to the mouth of the estuary) following the sample collection at WLI6 on day 2. To identify seasonal variability using a consistent dataset, the observations at stations CLIS and ARTG are not included in the discussion and visualizations of this manuscript but are included in the datasets archived to PANGAEA (Manning et al., 2026a; Manning et al., 2026b).

Water samples were collected from Niskin bottles attached to a rosette with a CTD (Sea-Bird Electronics SBE 9 with SBE 43 O_2 sensor). Additionally, to get near-bottom water at each station, a Niskin bottle was lowered by hand to approximately 1 m above the seafloor and manually closed. Seven depths were sampled at every station. The shallowest sample on each cast was collected at approximately 2 m depth and is hereafter referred to as the “surface” sample.

The water sample temperature, salinity, and O_2 concentrations reported in this paper and the accompanying datasets were taken from the sensor data corresponding to the time the bottle was closed (after at least 30 s of stabilization at a fixed depth). Due to the strong stratification of the system (median mixed layer depth 5 m), along with the slow response time (hysteresis) of the SBE43 O_2 sensor (Bittig et al., 2018; Martini et al., 2007) and the delayed response of the salinity sensor due to the internal pump, there were often offsets between the upcast and downcast that could not be eliminated even after accounting for these delays. On the downcast, the profiler was moving at roughly 1 m s^{-1} and the measured O_2 values lagged significantly behind the in situ values.

The temperature, salinity, and O_2 data for each near-bottom sample are taken from the CTD data matching with the deepest bottle closed on the corresponding rosette cast. Although a CTD and O_2 sensor attached to a frame without a rosette was deployed by hand to obtain a reading nearer to the bottom, the CTD frame stirred up sediment as it approached the seafloor, leading to erroneous salinity readings and making this method unreliable. O_2 was calibrated as described in section 2.3 and the other CTD sensors used the manufacturer’s calibration. Salinity is reported on the unitless practical salinity scale (PSS-78).

2.2 CH_4 and N_2O sample collection and analysis

Water samples for CH_4 and N_2O analysis (duplicates for each depth) were collected into 120 mL glass serum bottles using flexible PVC tubing, with at least three times the sample volume flowing through the bottle before the sample was sealed. Samples were preserved following published procedures: 0.5 mL of 8 M potassium hydroxide (KOH) was used in August (Magen et al., 2014) and 100 µL of 3.8 g L^{-1} mercuric chloride

solution (50% saturation) was used in October and May (Dickson et al., 2007). Experiments in our lab have demonstrated that these two preservation methods yield statistically equivalent and stable concentrations for CH_4 and N_2O over storage periods from 0 to 6 months (manuscript in preparation). Samples were sealed with bromobutyl rubber stoppers and aluminum crimp seals. Analysis was completed within 5 months of each cruise.

Samples were prepared for analysis using headspace equilibration (Magen et al., 2014; de la Paz et al., 2021). Approximately 22 mL of water sample was removed while the same volume of ultrahigh purity N_2 (5.0 grade) at ambient atmospheric pressure was added. The samples were shaken for 3 hours at room temperature. Then, approximately 20 mL of the headspace was transferred to a 12 mL pre-evacuated vial (Labco Exetainer) by injecting 20 mL of brine solution (105 mg L^{-1} NaCl) into the bottom of the sample bottle and inserting a needle into the headspace to transfer the headspace gas into the vial. The Exetainer was filled to >1 atm pressure to prevent air from entering the vial when the needle was removed. The Exetainers contained dried KOH to remove CO_2, which can interfere with the quantification of N_2O (Zheng et al., 2008).

Samples were analyzed using an SRI 8610C gas chromatograph with flame ionization detector (FID) for CH_4 and electron capture detector (ECD) for N_2O. An xyzTek Bandolero autosampler was used to transfer the sample into two loops in sequence, with a 2 mL loop going to the FID and 0.25 mL loop going to the ECD. The sample loop and autosampler tubing was evacuated to below 6 torr, and then a needle was injected into the Exetainer vial, allowing the sample gas to fill the evacuated loops. The injected gas in the sample loop equilibrated to atmospheric pressure before it was transferred to the column. The FID flow path included a HayeSep D pre-column followed by a Shincarbon column to optimize separation of O_2 and CH_4. For the ECD, there was a HayeSep D pre-column followed by two HayeSep D columns with a vent in between to prevent O_2 from reaching the detector. Backflushing the pre-columns prevented water vapor from entering the main separatory columns. For the FID we used N_2 as carrier gas, with hydrogen added to generate the flame, and for the ECD we used N_2 as carrier gas, with P5 (95% CH_4, 5% argon) added as makeup gas at the detector to increase sensitivity.

Samples were calibrated using an Airgas certified standard containing 9.82 ppm CH_4 and 7.97 ppm N_2O in N_2. The Airgas standard was calibrated internally using an air standard from the NOAA Carbon Cycles and Greenhouse Gas Group (Boulder, Colorado, USA) to reference all data to the WMO scale (Dlugokencky et al., 2020a; Dlugokencky et al., 2020b) with an accuracy of 1% for both CH_4 and N_2O. For each set of water samples run, a set of seven standards ranging from 0 ppm to 9.82 ppm CH_4 and 0 to 7.97 ppm N_2O was prepared by mixing the Airgas standard with pure N_2 using Alicat mass flow controllers and injecting each standard mixture into Exetainers. A linear calibration curve was used for CH_4 and a quadratic calibration curve was used for N_2O (Wilson et al., 2018).

Samples of deionized water equilibrated at room temperature were included in every analytical batch. Community reference materials for CH_4 and N_2O in water are not commercially available, and therefore, preparation of air-equilibrated water samples in house is currently recommended as a quality assurance measure (Wilson et al., 2018). Compared to expected results based on atmospheric gas concentrations in Mashpee, Massachusetts, USA (see section 2.4), the average error for these samples was 0.32 nmol kg^{-1} for CH_4 and 0.07 nmol kg^{-1} for N_2O. The median precision of duplicate field samples was 4 nmol kg^{-1} (7% relative standard deviation) for CH_4 and 0.3 nmol kg^{-1} (3% relative standard deviation) for N_2O.

2.3 O_2 sample collection and analysis and correction of in situ O_2 data

Discrete samples for O_2 concentration measurement were collected on several casts on each cruise. Duplicate or triplicate samples were collected into 140 mL glass biological oxygen demand (BOD) flasks with

flared necks using flexible PVC tubing, with at least three times the sample volume flowing through the bottle before the sample was sealed. O_2 samples were preserved by adding 1 mL of $MnCl_2$ solution and 1 mL of NaI-NaOH solution before inserting a ground glass stopper (Langdon, 2010). The flared neck was filled with water, and the neck and stopper were covered with a latex rubber seal to keep the stopper in place and reduce evaporation. Samples were stored in the dark prior to analysis, which occurred within a few days of each cruise. Analysis was performed via amperometric Winkler titration with a precision of 0.3% based on the standard deviation of replicate samples (Langdon, 2010). The discrete O_2 sample data was used to apply a linear correction factor to the SBE 43 O_2 sensor data for each cruise.

2.4 Equilibrium concentrations and sea-air flux calculations

In this manuscript, we report the saturation anomaly, Δ, as the concentration or percentage over or undersaturation (depending on context). For O_2:

$$\Delta O_2, \mu\text{mol kg}^{-1} = [O_2]_{\text{meas}} - [O_2]_{\text{eq}} \quad (1)$$

$$\Delta O_2, \% = \frac{[O_2]_{\text{meas}} - [O_2]_{\text{eq}}}{[O_2]_{\text{eq}}} \times 100\% \quad (2)$$

Here $[O_2]_{meas}$ and $[O_2]_{eq}$ are the measured and equilibrium concentrations of O_2, respectively. Equilibrium concentrations were calculated from the measured temperature and salinity following Wiesenburg and Guinasso (1979) for CH_4 and Weiss and Price (1980) for N_2O using MATLAB functions by Manning and Nicholson (2026). All gas concentrations are reported in molal units (mol kg^{-1}) to allow the gases to be used as conservative tracers, following the conventions of the Global Ocean Ship-Based Hydrographic Investigations Program (GO-SHIP) and Biogeochemical Argo (Bittig et al., 2018; Thierry et al., 2025).

Sea-air gas flux was calculated for CH_4 as follows, and an analogous approach was used for N_2O

$$F = k\left([CH_4]_{\text{meas}} - [CH_4]_{\text{eq}}\right). \quad (3)$$

Here positive values indicate a net sea to air flux (i.e., outgassing), and *k* is the gas transfer velocity calculated with the equation of Wanninkhof et al. (2014), which is a function of the wind speed at 10 m height and the Schmidt number (ratio of the seawater kinematic viscosity to the gas diffusivity). The Schmidt number is calculated for CH_4 following Jähne et al. (1987) and for N_2O following Wanninkhof (2014), which uses coefficients based on prior publications by Hayduk and Laudie (1974) and Wilke and Chang (1955).

For calculating equilibrium concentrations, the dry atmospheric concentrations of CH_4 and N_2O were set to 2020 and 338 ppbv, respectively. These concentrations are taken from preliminary surface flask measurements from Mashpee, Massachusetts, USA (station MSH) from the NOAA Carbon Cycle Greenhouse Gases group website (https://gml.noaa.gov/ccgg/) and represent the average over the three cruises (Dlugokencky et al., 1994; Hall et al., 2007; Dlugokencky et al., 2020b; Dlugokencky et al., 2020a; Lan et al., 2021). Final surface flask results were not available at the time of dataset submission to PANGAEA, but small changes in the atmospheric concentration of both gases would have a negligible impact on the calculated equilibrium concentrations and sea-air fluxes, relative to other sources of error in the measurements and calculations. Final CH_4 data from station MSH were made available after dataset publication and indicate that the atmospheric concentration was 0.2% higher (2024 ppbv). This difference is much smaller than the measurement uncertainty (e.g., 7%, the mean relative standard deviation for duplicate samples). The dry atmospheric concentrations were adjusted to wet concentrations by assuming 100% relative humidity at the air-sea interface and adjusted to local sea level pressure using the mean sea level pressure from the 15 days prior to each measurement, obtained from a mooring at station EXRX, NOAA buoy 44022 (US Department of

Commerce, 2025). Wind speed was measured on the same mooring and extrapolated from the measurement elevation of 3.5 m to 10 m following Hsu et al. (1994).

Because gas transfer velocity is a non-linear function of wind speed, higher wind speeds have a disproportionate effect on the total flux, and therefore gas fluxes calculated based on average wind speeds will underestimate the true flux and fluxes based on instantaneous wind speeds can be biased high or low (Wanninkhof et al., 2009). In the archived dataset, we report fluxes calculated by two different methods: using instantaneous winds (15 min average), and using a time-weighted approach incorporating winds up to 15 days prior to sampling (Manning et al., 2026b). The weighted approach follows the equation of Teeter et al. (2018), which is modified from Reuer et al. (2007).

$$k = \frac{\sum_{t=1}^{n} k_t\, \omega_t}{\sum_{t=1}^{n} \omega_t} \tag{4}$$

$$\omega_n = 1,\ \omega_i = \omega_{i+1}(1 - f_{i+1}) \tag{5}$$

$$f_i = \frac{k_i \Delta t}{MLD} \tag{6}$$

In equation 4, t is the time index, with $t = n$ representing the time of sampling, and $t = 1$ occurring 15 days prior. The term k_t refers to the gas transfer velocity (m s^{-1}) at time step t, and ω_t is the weighting at index t (ranging from 0 to 1). The variable f_i is the fraction of the mixed layer ventilated at index i, ω_i is the weighting coefficient at index i, MLD is the mixed layer depth, and Δt is the time interval between each wind speed measurement (15 min in this study). We use a time interval of 15 min so that $f_i \leq 1$ at every time point, despite the shallow mixed layer depths. The weighting coefficient decreases going back in time, since it is the product of the current weighting coefficient and the previous weighting coefficient (always ≤ 1), and also decreases when the gas transfer velocity decreases.

The mixed layer depth was defined using CTD profiles that were averaged into 1 m depth bins, based on a density difference criterion of 0.125 kg m^{-3} relative to the shallowest bin (centered at 2 or 3 m). The mixed layer depth was assumed to be constant in time for the flux calculation. Mixed layer depths ranged from 3–14 m (median 5 m, mean 5.8 m).

A weighting period of 15 days was selected due to the shallow mixed layer depth. The mean residence time of both CH_4 and N_2O was 4 days (calculated from the ratio of the mixed layer depth to the gas transfer velocity). Additionally, the meteorological sensors on the buoy at EXRX malfunctioned beginning in September 2023 and were replaced 16 days prior to the October cruise. For this reason, a longer weighting period in October was not possible. For May and August, where 30 days of wind speed data was available prior to the cruise, we compared the gas transfer velocities calculated using a weighting period of 15 and 30 days and found that they agreed within 3%.

In this manuscript, we focus on the time-weighted flux results, consistent with many other publications reporting CH_4 and N_2O fluxes, because this method better reflects the typical gas flux occurring over multiple days in each season, and allows for more robust seasonal comparisons (Townsend-Small et al., 2014; Capelle et al., 2019; Zhan et al., 2021; Manning et al., 2022; Schuler and Tortell, 2023). In August, the instantaneous fluxes were on average four times lower than the weighted fluxes, whereas in May the instantaneous fluxes were on average three times higher than the weighted fluxes, due to short-term variability in wind speeds.

Typical uncertainty in sea-air gas fluxes was estimated to be 24% for CH_4 and 26% for N_2O using a Monte Carlo error analysis that incorporated the largest known sources of uncertainty (quantified here as relative standard deviation): the parameterization of k as a function of wind speed, at 20% per Wanninkhof et al. (2014); the measured wind speed, at 3% per the sensor manufacturer's specifications; and the gas concentration, at 12% for CH_4 and 4% for N_2O. The uncertainty in the gas concentrations is estimated based

on the relative standard deviation of repeat measurements at station MID4 collected during each cruise; this reflects uncertainty in the fluxes driven by short-term variability in gas concentrations that was not captured by the instantaneous sampling. The uncertainty due to instantaneous sampling is greater than the analytical uncertainty (reproducibility of duplicates). One potential systematic error that is not captured in our error estimates is lateral variability in wind speed along the transect, which could not be quantified as wind speed data was only available at station EXRX. Additionally, we decided to use the parameterization of Wanninkhof et al. (2014), which was developed using open ocean data, rather than a parameterization developed for riverine or estuarine systems. Ho et al. (2011) conducted a tracer release study in the Hudson River (a tidally-influenced river that partially flows into the East River) and found that a wind speed-based parameterization developed for the open ocean was accurate in this system; the effect of bottom turbulence was negligible. Given the deeper depth in our study region (13–32 m) as compared to the average depth of 6 m in the Hudson River study, we expect bottom turbulence to play a smaller role in western LIS. Currently, scientists lack a broad consensus on the appropriate gas exchange parameterization for estuarine systems due to the variable impacts of factors including wind speed, fetch, currents, bottom-driven turbulence, turbidity, and surfactants (Raymond and Cole, 2001; Borges et al., 2004; Upstill-Goddard, 2006; Abril et al., 2009). Our estimated uncertainties in the gas fluxes represent a lower limit.

3. Results and Discussion

3.1 Seasonal and spatial trends in hydrography

The sampling months were chosen to reflect the annual variability in hydrographic properties in western LIS. We sampled in August 2023 (near the annual maximum extent of hypoxia), October 2023 (following seasonal ventilation of the subsurface), and May 2024 (near peak river inflow and prior to the onset of hypoxia). Progressive cooling and freshening occurred from August through May. Specifically, in August, temperature ranged from 20.1 to 24.1°C and salinity from 26.0 to 27.0, in October, temperature ranged from 17.0 to 18.1°C and salinity from 24.7 to 26.5, and in May, temperature ranged from 11.4 to 17.9°C and salinity ranged from 22.4 to 24.2 (Figure 2). Our hydrographic data are consistent with prior observations, which showed the annual minimum salinity in LIS typically occurs in May and is associated with peak river discharge (Lee and Lwiza, 2005; O'Donnell et al., 2008; O'Donnell et al., 2014).

Using transect data at the depths sampled for gases, the in situ temperature was 21.6 ± 0.9°C in August, 17.4 ± 0.4°C in October, and 13.6 ± 1.8°C in May (mean ± standard deviation). Salinity was 26.63 ± 0.27 in August, 25.71 ± 0.52 in October, and 23.39 ± 0.49 in May. October displayed the least stratification, and May displayed the strongest stratification and shallowest mixed layer depths (Figure 3j-l). In October, the thermal gradient reached a minimum, with surface waters typically displaying a lower temperature than the subsurface (mean surface temperature of 17.1°C; and mean temperature below 10 m of 17.7°C). Seasonal cooling due to changes in surface heat flux causes a decline in temperature and stratification over fall and winter (Lee and Lwiza, 2008; O'Donnell et al., 2014).

Generally, density and salinity increased from west to east throughout the water column (Figure 3j-o), consistent with prior observations and reflecting the influence of the low salinity waters discharged from the East River (Lee and Lwiza, 2005; O'Donnell et al., 2008). Within the East River, there is two-layer estuarine flow with net surface transport toward LIS and subsurface transport toward New York Harbor, though the flow direction can temporarily reverse (Blumberg and Pritchard, 1997; Gay et al., 2004). For example, in October, salinity increased from 24.68 at EXR1 to 25.86 at WLIS and 25.74 at WLI6. One notable outlier from these trends was found at station EXRX in May. In May on day 2, when the transect was collected, EXRX displayed

the highest surface density anomaly out of all the stations (16.8 kg m^{-3}), in comparison to 16.0 kg m^{-3} at EXR1 to the west and 16.0 to 16.3 kg m^{-3} at the remaining stations to the east. The surface temperature was significantly lower at EXRX (14.5ºC), as compared to 16.2 to 17.3ºC at all other stations. The surface salinity at EXRX was 22.88, which fell between the values at the easternmost stations WLIS (22.86) and WLI6 (23.03) and was significantly higher than EXR1 (22.38). The mixed layer depth at EXRX was 7 m, as compared to 3 to 5 m at the remaining stations. Notably, when sampled in May on day 1 of the cruise, EXRX displayed a surface salinity of 22.35, temperature of 16.0 ºC, and density anomaly of 16.1 kg m^{-3}, and a mixed layer depth of 4 m (Manning et al., 2026a). Overall, these results suggest the temporary presence of a distinct mixed layer water mass at EXRX in May on day 2 of the cruise.

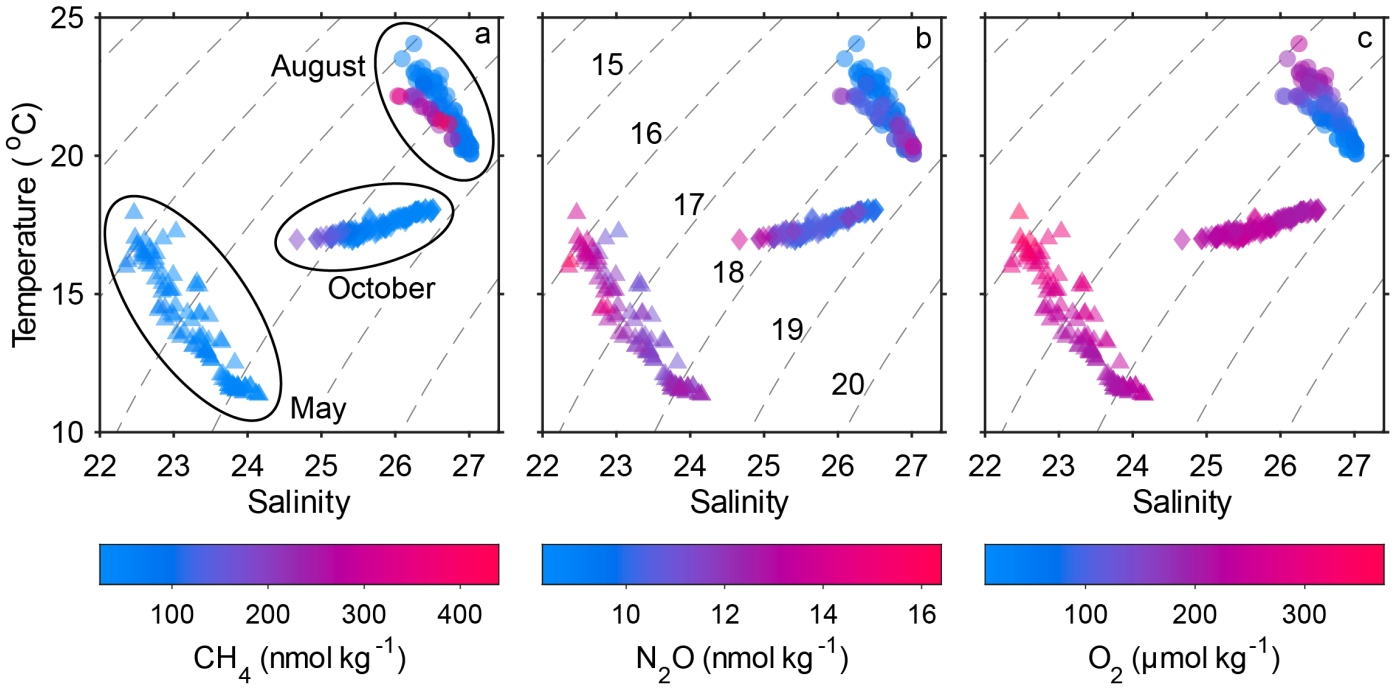

Figure 2. Temperature-salinity plot showing water mass distributions of CH_4, N_2O, and O_2 concentrations.
CH_4 concentration (a), N_2O concentration (b) and O_2 concentration (c) during August (circles), October (diamonds) and May (triangles). In panel a, ellipses indicate the cluster of data points from each month. Dashed lines represent the density anomaly (kg m^{-3}), labelled in panel b. Here, all data from all stations are included, including repeat profiles at MID4 and EXRX. Salinity is reported on the unitless practical salinity scale (PSS-78).
Alt Text: Scatter plot of dissolved gas concentrations (CH_4, N_2O, and O_2) visualized as a function of temperature and salinity. The data show distinct water masses were present in each sampling month, with August showing the highest temperature.

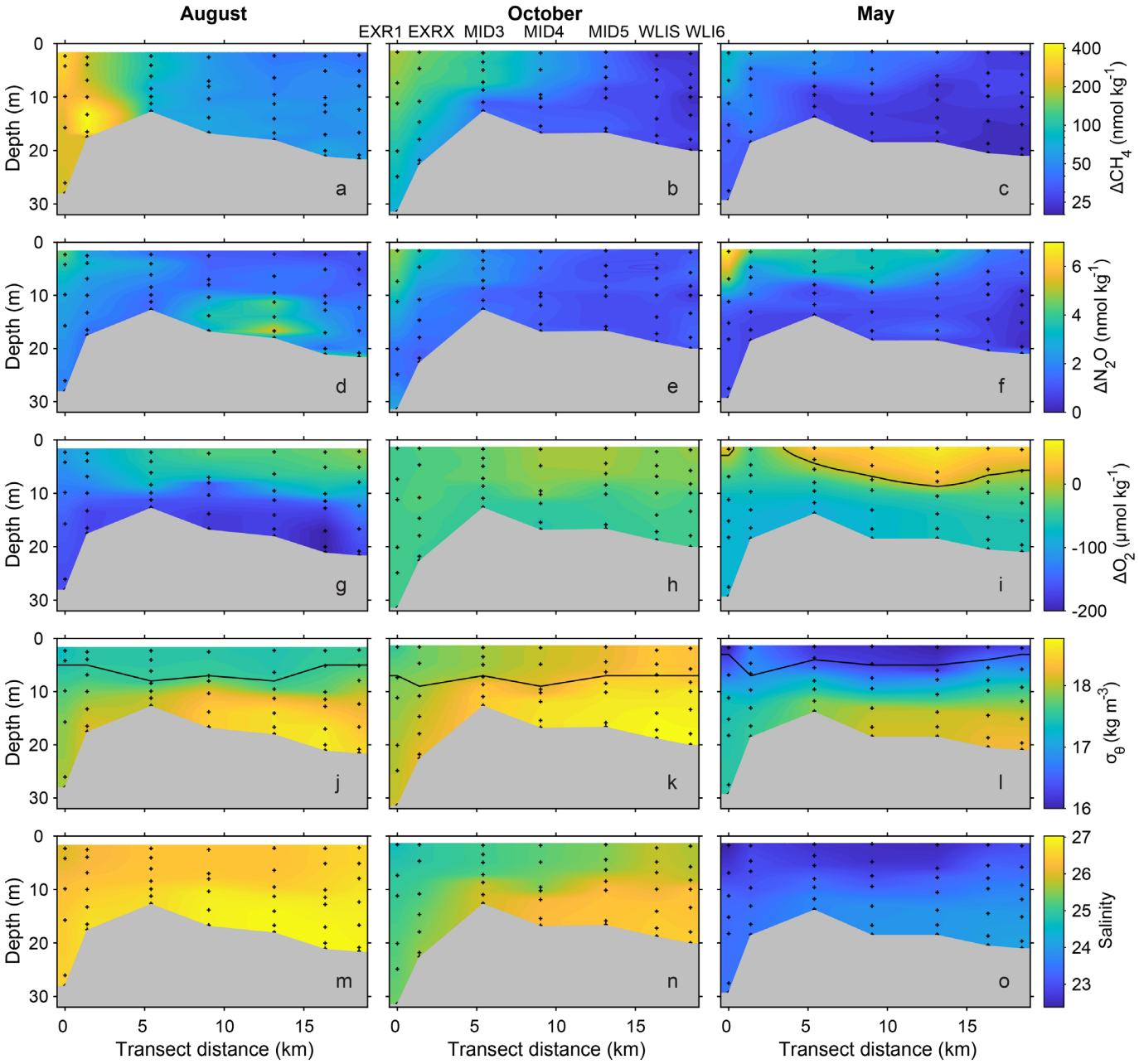

Figure 3. Measurements of dissolved gases and other parameters along the transect in western LIS.
The first three rows show gas saturation anomalies: ΔCH_4 in nmol kg^{-1} (a–c), ΔN_2O in nmol kg^{-1} (d–f), and ΔO_2 in μmol kg^{-1} (g–i). The fourth row is the potential density anomaly in kg m^{-3} (j–l) and the bottom row is the salinity (m–o). Note that ΔCH_4 is plotted using a logarithmic scale bar to better display the lateral gradients in each season. The black line on panel i represents equilibrium (ΔO_2 = 0 μmol kg^{-1}); O_2 was undersaturated at all stations along the transect in August and October. In the density plots (j–l), the solid line represents the mixed layer depth. The sampling depths are indicated with black circles, and the station names are labelled above panel b. . Reference Figure 1 for the position of the transect.
Alt Text: Depth section contour plots of dissolved gas saturation anomalies (CH_4, N_2O, and O_2), potential density anomaly, and salinity measured in August, October, and May along the seven-station transect shown in Figure 1.

3.2 Seasonal and spatial trends in CH_4, N_2O, and O_2 along the transect in western LIS

Over the three cruises, along the entire transect and all depths, CH_4 concentrations ranged from 25–438 nmol kg^{-1} (saturation anomaly 740–18000%), N_2O concentrations ranged from 8.4–16.3 nmol kg^{-1} (saturation anomaly 2–73%), and O_2 concentrations ranged from 8–372 µmol kg^{-1} (saturation anomaly −96–46%) as reported in Table 1 and visualized in Figure 3a–i. On average across the transect, CH_4 concentrations and saturation anomalies were highest in August (mean 119 nmol kg^{-1}, 4900%) and lowest in May (mean 38 nmol kg^{-1}, 1200%). Mean N_2O concentrations were highest in May (mean 12.0 nmol kg^{-1}) and lowest in August (mean 10.1 nmol kg^{-1}), whilst the mean N_2O saturation anomaly was highest in August (mean 31%) and similar in October and May (mean 19% in October and 18 % in May). Mean O_2 concentrations and saturation anomalies were lowest in August (mean 110 µmol kg^{-1}, −52%) and increased to similar levels in October (mean 220 µmol kg^{-1}, −13%) and May (mean 240 µmol kg^{-1}, −13%). However, O_2 was more homogeneous in October (the saturation anomaly had a standard deviation of 5% and O_2 was undersaturated at all depths), compared to May (the saturation anomaly had a standard deviation of 15% and reached a maximum of 24%), consistent with a less stratified water column in October (section 3.1).

Table 1. Temperature, salinity, and gas distributions incorporating measurements along the transect in western LIS from EXR1 to WLI6.

Parameter	August		October		May	
	Median[a]	Mean[b]	Median[a]	Mean[b]	Median[a]	Mean[b]
Temperature (°C)	21.4 (20.9, 22.3)	21.6 ± 0.9	17.3 (17.1, 17.9)	17.4 ± 0.4	13.3 (11.8, 15.2)	13.6 ± 1.8
Salinity[c]	26.6 (26.4, 26.9)	26.6 ± 0.3	25.6 (25.3, 26.2)	25.7 ± 0.5	23.4 (23.0, 23.8)	23.4 ± 0.5
CH_4 concentration (nmol kg^{-1})	68 (58, 194)	119 ± 101	43 (32, 98)	67 ± 44	32 (29, 45)	38 ± 13
CH_4 saturation anomaly (%)	2700 (2300, 8100)	4900 ± 4200	1500 (1200, 3600)	2400 ± 1600	1000 (900, 1500)	1200 ± 500
N_2O concentration (nmol kg^{-1})	9.8 (9.3 10.8)	10.1 ± 1.1	10.2 (9.9, 11.0)	10.5 ± 1.0	11.6 (11.4, 12.5)	12.0 ± 1.1
N_2O saturation anomaly (%)	27 (21, 37)	31 ± 13	16 (13, 22)	19 ± 10	11 (8, 23)	18 ± 15
O_2 concentration (µmol kg^{-1})	89 (69, 159)	110 ± 52	217 (210, 231)	220 ± 14	231 (211, 260)	240 ± 34
O_2 saturation anomaly (%)	−62 (−71, −31)	−52 ± 23	−14 (−16, −8)	−13 ± 5	−19 (−26, −3)	−13 ± 15

[a] Values in parentheses represent the first and third quartile, respectively.

[b] Uncertainty is the standard deviation. N = 106 in each month.

[c] Salinity is reported on the unitless practical salinity scale (PSS-78).

The clearest and most seasonally consistent spatial trend in gas concentrations along the transect was that the concentrations of CH_4 and N_2O from the surface to approximately 10 m were highest at the westernmost station, EXR1, and generally decreased eastward, and conversely, O_2 showed the opposite trend (Figure 3). Lateral gradients in O_2 in LIS and more severe O_2 depletion in the far western reaches of LIS are both annual features of the O_2 dynamics in LIS (O'Donnell et al., 2014; Whitney and Vlahos, 2021). One exception to this trend is in May 2024 where the westernmost station EXR1 had a higher surface O_2 concentration compared to the adjacent station EXRX (276 µmol kg^{-1} at EXR1 compared to 233 µmol kg^{-1} at EXRX). The remaining stations in this transect, to the east of EXRX, had higher and similar O_2 concentrations

(290 to 323 μmol kg^{-1}). However, the CH_4 and N_2O concentrations at EXR1 and EXRX followed the expected west-east gradient in May (i.e., EXR1 displayed the highest surface concentrations of CH_4 and N_2O). As discussed in section 3.1, there appeared to be a distinct surface water mass at EXRX in May.

Although O_2 decreased with depth at each station in the transect in all three months, the vertical gradients in CH_4 and N_2O were more variable (Figure 3). In October and May, five to seven of the seven stations had higher CH_4 and N_2O concentrations at the surface than the bottom. In August some stations had both surface and subsurface CH_4 and N_2O peaks and the positions of CH_4 and N_2O maxima were notably not coincident. The easternmost stations WLIS and WLI6 consistently displayed the lowest surface CH_4 and N_2O concentrations and the smallest vertical ranges in CH_4 concentration. In comparison with N_2O, CH_4 displayed a larger range in concentration and saturation anomaly across the entire transect as well as a larger range in concentration and saturation anomaly at individual stations on each cruise.

The transect measurements shown in Figure 3 were collected over an approximately 6 h period on each cruise beginning near 08:00 local time. We are unable to evaluate the contribution of temporal differences to the observed spatial trends, given that we only collected one profile at five of the seven stations on each cruise. However, in all three months we observed an enrichment in near-surface CH_4 and N_2O concentrations at the westernmost station (with concentrations decreasing eastward) and depletion in near-surface O_2 concentrations at the westernmost station (with concentrations increasing eastward), giving us confidence that these features are persistent.

3.3 Diel variability in CH_4, N_2O, and O_2 observed in repeat measurements at MID4

To characterize temporal evolution in CH_4, N_2O, and O_2 on sub-daily timescales, we sampled at station MID4 eight times on each cruise (every 4 hours beginning near 08:00 on day 1). We used tidal current speed predictions generated by NOAA for 3, 9, and 14 m depth at station LIS1035 (200 m from MID4, Figure 1) to determine the direction of water flow resulting from the semidiurnal tides at MID4 (Bennett et al., 2010; McCardell et al., 2016; Duvall et al., 2024). These predictions have a mean error of 8 minutes or less in the timing of flood, slack and ebb, and current speed root mean square error of 0.04 m s^{-1} (NOAA, 2025). The current predictions indicate that at MID4 during flood tide (positive current speeds), the water flows toward the East River, with a mean flood current direction of 233° at 3 m, 244° at 9 m, and 251° at 14 m. The timing of flood and ebb tides varied with depth. During our three cruises, the peak flood tide (maximum positive current speed on each tidal cycle) occurred first at 14 m, and an average of 18 min later at 9 m, and 38 min later at 3 m (Figure 4a–c). We applied a linear interpolation to the discrete sample data from each profile to estimate the gas concentrations at 3, 9, and 14 m, matching the depths of the tidal current predictions. We then investigated the relationship between tidal stage and interpolated gas concentrations at these three depths.

The concentration of O_2 at MID4 varied with season, depth, and time of day (Figure 4j-l). O_2 concentrations were highest in May (mean of 317 μmol kg^{-1} at 3 m and 212 μmol kg^{-1} at 14 m) and lowest in August (mean of 196 μmol kg^{-1} at 3 m and 49 μmol kg^{-1} at 14 m), matching the seasonal trends across all stations. The variability observed in O_2 at 3 m depth at MID4 over the 28 h repeat sampling was largest in May (range of 87 μmol kg^{-1}, from 276 to 363 μmol kg^{-1}), intermediate in August (range of 37 μmol kg^{-1}, from 179 to 216 μmol kg^{-1}), and smallest in October (range of 27 μmol kg^{-1}, from 231 to 258 μmol kg^{-1}). These trends are consistent with the east-west range in O_2 observed along the transect at 3 m depth (Figure 3g-i), which was also largest in May (84 μmol kg^{-1}) and smallest in October (30 μmol kg^{-1}). The range in O_2 at MID4 observed in each month consistently decreased with depth. For example, the range in O_2 in May was 87 μmol kg^{-1} at 3 m depth, 54 μmol kg^{-1} at 9 m depth, and 13 μmol kg^{-1} at 14 m depth.

At MID4, mean CH_4 concentrations were highest in August (55, 64, and 68 nmol kg^{-1} at 3, 9, and 14 m depth, respectively) and lowest in May (46, 30, and 29 nmol kg^{-1} at 3, 9, and 14 m depth, respectively), as shown in Figure 4d–f. Conversely, mean N_2O concentrations were highest in May (12.9, 11.6, and 11.7 nmol kg^{-1} at 3, 9, and 14 m depth, respectively), and lowest in August (8.9, 9.9, and 10.2 nmol kg^{-1} at 3, 9, and 14 m depth, respectively), as shown in Figure 4g–i. For both gases, the seasonal trends at MID4 were consistent with the seasonal trends across the entire transect (Table 1). For each of the three depths evaluated, in each of the three months, the CH_4 concentration at MID4 varied by 6 to 25 nmol kg^{-1} over 28 h, and the N_2O concentration varied by 0.4 to 2.2 nmol kg^{-1} over 28 h. Unlike for O_2, we did not observe a consistent decrease in the variability of CH_4 and N_2O with depth in each month. For example, for N_2O, the variability at MID4 was largest at 14 m depth in August and October (2.0–2.2 nmol kg^{-1}) and largest at 3 m depth in May (2.0 nmol kg^{-1}), whereas the lateral variability along the entire transect was largest at 3 m in all three months (3.3–5.3 nmol kg^{-1}) as compared to 9 and 14 m.

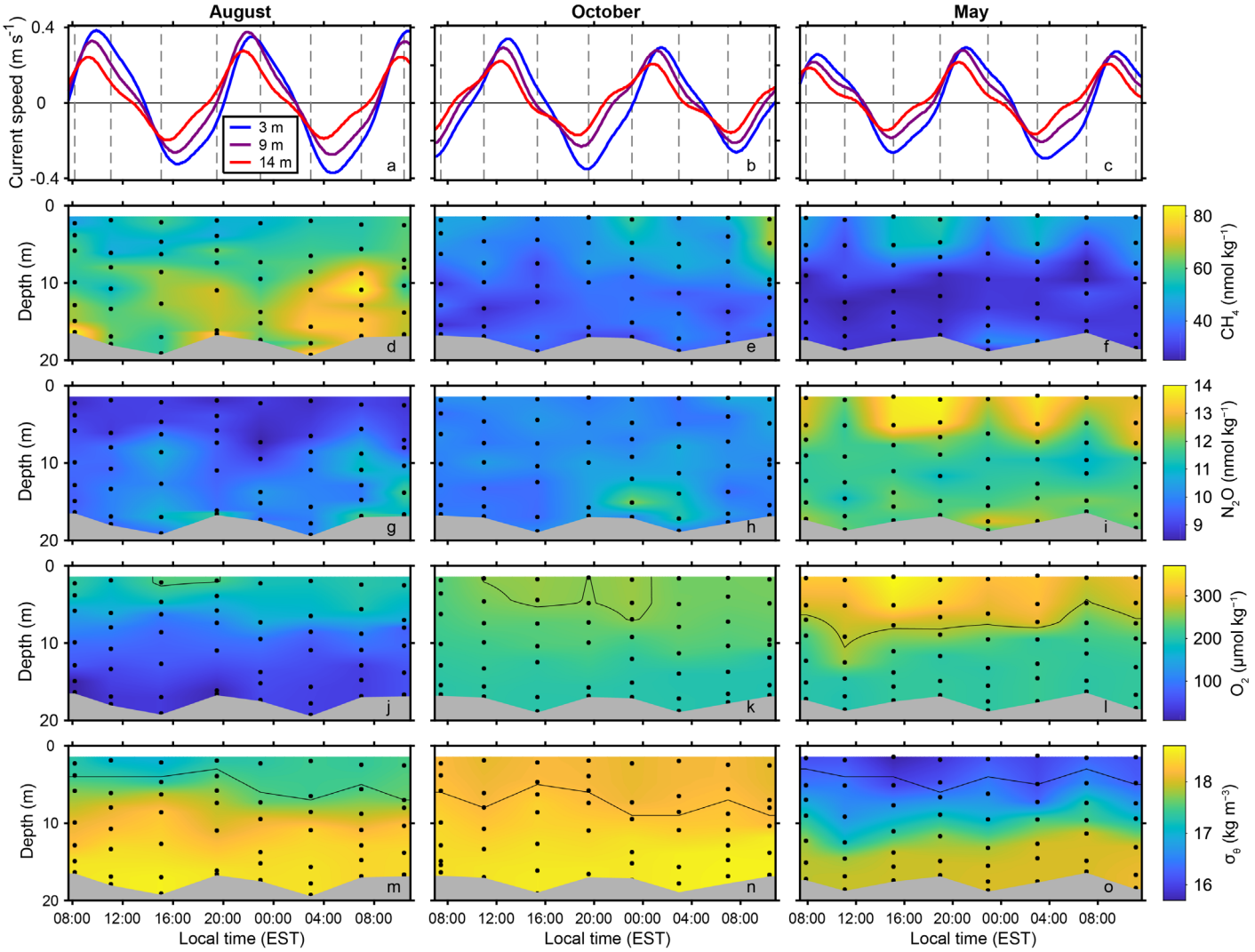

Figure 4. Time-series of repeat measurements at MID4 collected over 28 h in each month.
Predicted current speed in m s^{-1} at 3, 9, and 14 m depth (blue, purple, and red lines, respectively) at station LIS1035, near MID4 (a–c) on August 2–3, 2023 (a), October 19–20, 2023 (b) and May 22–23, 2024 (c). Vertical dashed lines indicate sampling times. Here, positive current speeds indicate flow toward the southwest (flood tide, increasing water depth). Dissolved gas concentrations in samples collected at station MID4 every 4 h for 28 h: CH_4 in nmol kg^{-1} (d–f), N_2O in nmol kg^{-1} (g–i), O_2 in µmol kg^{-1} (j–l), and potential density anomaly in kg m^{-3} (m–o). Black circles indicate sampling times and depths. Measured bottom depth is variable due to the 2 m tidal range at this site. In the O_2 plots (j–l), the solid black line represents equilibrium (depths above the line are supersaturated), and in the density plots (m–o) the solid line represents the mixed layer depth.

Alt Text: Top panel displays predicted current speeds in August, October, and May at station LIS1035, with a range of −0.4 to 0.4 m s^{-1}. Lower panels display time series of CH_4, N_2O, and O_2 concentrations and potential density anomaly at station MID4.

To further evaluate the influence of diel changes in light and tidal stage on the dissolved gas data, we visualized the MID4 profiles relative to the time of local solar noon (approximately 13:00, varying by month) and relative to tidal phase (peak flood tide) in Figures 5 and 6, respectively. For the evaluation of light effects, we focus our discussion on results at 3 m depth because the daily range in light is largest at this depth. From biological processes alone, we would expect near-surface O_2 to be highest near sunset due to the accumulation of photosynthetic O_2 during the day, and lowest near sunrise, due to the lack of photosynthesis and continued respiratory consumption overnight (Nicholson et al., 2015; Izett et al., 2024). At 3 m depth, the minimum O_2 concentration in October (231 μmol kg^{-1}) and May (276 μmol kg^{-1}) occurred in the sample collected closest to sunrise, as would be expected for a biologically dominated diel signal (Figure 5). However, in August, the minimum O_2 concentration (179 μmol kg^{-1}) occurred at 2 h before solar noon, with three profiles collected earlier in the morning but after sunrise showing a higher O_2 concentration (193–204 μmol kg^{-1}). In all three months, the maximum O_2 concentration at 3 m depth occurred 2–3 hours after local solar noon, but in all cases, there was a profile collected closer to sunset with a lower O_2 concentration at 3 m. Thus, our sampling at 4 h resolution suggests that near-surface O_2 is likely varying in response to diel changes in photosynthesis rates, but that other factors must also be important drivers. At 9 and 14 m, there was also a lack of consistent relationship with time of day.

The expected diel light-driven cycle in CH_4 and N_2O concentrations in western LIS was not known a priori, given that the relative importance of different light-dependent sources and sinks was unknown. For example, nitrification rates are inhibited by light and enhanced by increases in NH_4^+ availability, which can vary daily due to changes in phytoplankton demand (Smith et al., 2014; Proctor et al., 2023). Other studies indicate that both CH_4 and N_2O can be produced in surface waters through photochemical reactions (Tang et al., 2014; Li et al., 2020; Leon-Palmero et al., 2025). At 3 m depth, the minimum CH_4 concentration over 28 h of sampling occurred at 6.5, 2.7, and −1.8 h relative to solar noon in August, October, and May, respectively, while the maximum CH_4 concentration occurred at −2.6, −2.3, and 6.1 h relative to local solar noon in August, October, and May, respectively (Figure 6). At 3 m depth, the minimum N_2O concentration occurred at −10.1, −9.7 and −1.8 h relative to local solar noon in August, October and May, respectively, while the maximum N_2O concentration occurred at −6.0, −2.3, and 6.1 h relative to local solar noon in August, October, and May, respectively. We conclude that light variability is not the primary driver of daily variability in near-surface CH_4 and N_2O at MID4. For O_2, CH_4, and N_2O, we did not observe any consistent relationships between dissolved gas concentrations and time of day at 9 and 14 m.

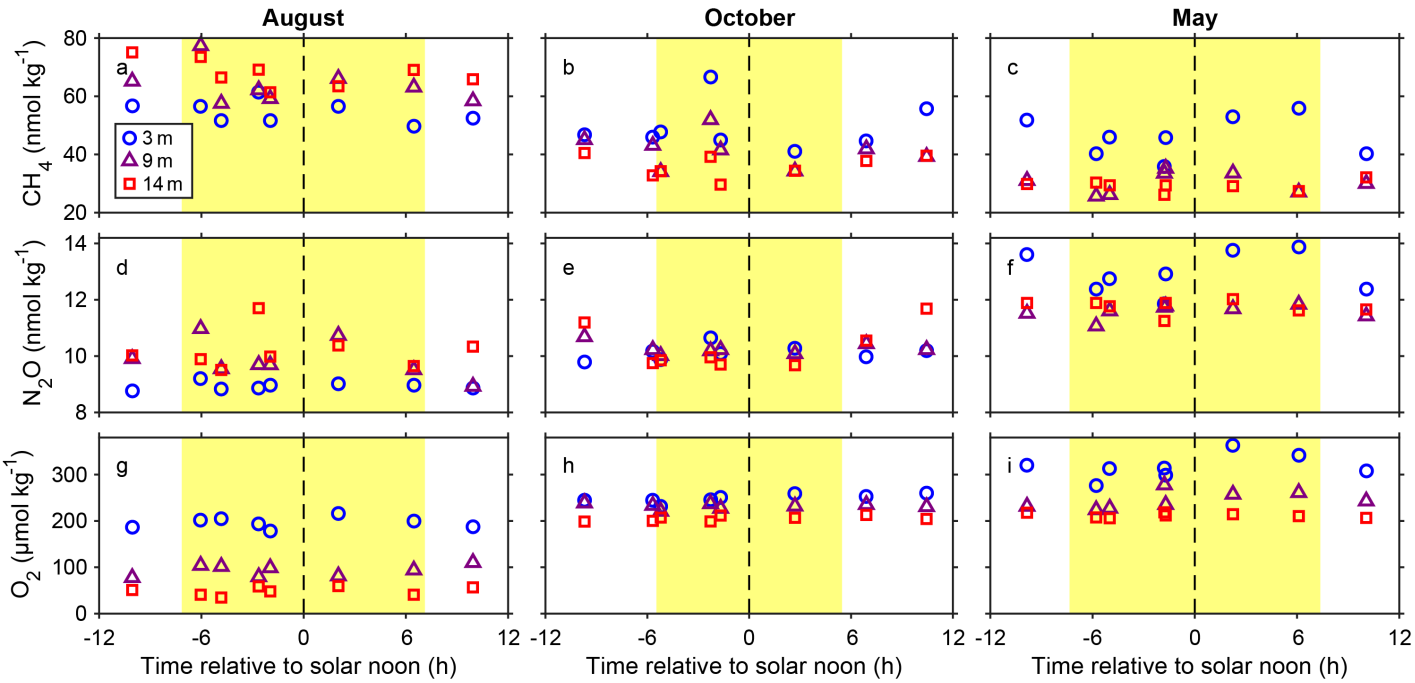

Figure 5. Dissolved gas concentrations at MID4 relative to the timing of solar noon.
Concentrations of CH_4 in nmol kg^{-1} (a–c), N_2O in nmol kg^{-1} (d–f) and O_2 in µmol kg^{-1} (g–i) in August (left), October (center) and May (right column). Blue circles, purple triangles, and red squares represent 3, 9, and 14 m depth, respectively. The yellow shaded area is the period from sunrise to sunset.
Alt Text: Timeseries of dissolved gas concentrations (CH_4, N_2O, and O_2) at station MID4 for each cruise, visualized as a function of time relative to solar noon.

To investigate the gas variability relative to tidal phase, we defined the peak flood tide (maximum positive current speed in each tidal cycle) as 0 h and then calculated the time of each profile relative to the closest peak flood (Figure 6). Given the semidiurnal tides at this site, peak ebb will occur at approximately −6.2 h and 6.2 h relative to peak flood. Low and high tide occur at −3.1 h and 3.1 h relative to peak flood, respectively (slack water, current speed of 0 m s^{-1}).

Surface concentrations of CH_4 and N_2O were highest (and O_2 lowest) at the southwestern stations. Therefore, if the observed variability in near-surface gas concentrations was predominantly driven by lateral advection associated with the tides, we would expect CH_4 and N_2O concentrations at 3 m to be lower (and O_2 higher) during periods when water at MID4 had originated from the northeastern sound, i.e., near high tide, the end of the flood current (approximately 3.1 h). Similarly, we would expect CH_4 and N_2O concentrations to be higher (and O_2 lower) near low tide, the end of the ebb current (approximately −3.1 h).

At 3 m depth, the minimum O_2 concentration occurred at 1.2, −5.5, and −2.4 h relative to peak flood, and the maximum concentration occurred at 5.2, −2.4, and −6.0 h relative to peak flood in August, October and May, respectively. Thus, only the timing of the minimum O_2 concentration in May (−2.4 h) followed the expected trend for a lateral advection-dominated signal.

At 3 m, the maximum concentrations of both CH_4 and N_2O occurred at −3.4 h relative to peak flood in October, and −2.1 h relative to peak flood in May. In August, the maximum CH_4 concentration at 3 m occurred at −0.4 h relative to peak flood and the maximum N_2O concentration occurred at −3.8 h relative to peak flood. Thus, the timing of all but the maximum CH_4 concentration in August were consistent with variability driven by tidal advection. This result is notable because the east-west CH_4 gradient in surface waters was largest in August and therefore we might have expected August to display the largest sensitivity to tidal advection. The minimum concentrations of CH_4 and N_2O occurred between 1.4 to 2.4 h relative to peak flood in October and May. In August, the CH_4 minimum occurred at −2.8 h relative to peak flood and the N_2O minimum occurred at

4.7 h relative to peak flood. Therefore, the timing of the near-surface CH_4 and N_2O minima in October and May was generally consistent with a horizontal advection-dominated signal, but the timing in August was not.

Vertical mixing associated with tides may also influence dissolved gas concentrations. For example, studies using continuous mooring data in western LIS reported that tides contribute to both vertical mixing and lateral O_2 transport. In summer, flood tides can result in vertical transport of well-oxygenated water deeper in the water column, increasing near-bottom O_2 and reducing vertical gradients in O_2 (McCardell et al., 2016; Duvall et al., 2024). However, in this study, at 14 m depth, we again did not see a consistent relationship between tidal phase and O_2 concentrations; the maximum O_2 concentration occurred at 5.8, −5.3, and 2.9 h relative to peak flood tide in August, May, and October, respectively. For CH_4 and N_2O, the vertical gradient in concentration varied between profiles in a single cruise. For example, in August, CH_4 and N_2O concentrations were always lowest at 3 m, but there was sometimes a subsurface peak at 9 m, and sometimes a peak at 14 m. In contrast, the O_2 concentration was always highest at 3 m and lowest at 14 m in August. Given the lack of a consistent vertical gradient in CH_4 and N_2O at MID4, we expect that the effect of vertical tidal mixing on CH_4 and N_2O concentrations will vary with time and with season and be smaller than is observed for O_2.

Our observations at MID4 suggest that the drivers of variability in CH_4, N_2O, and O_2 are complex and cannot be correlated to light levels or tidal phase alone. Similarly, Duvall et al. (2024) found that at station EXRX, O_2 was influenced by both the diel variability in photosynthesis rates and tides. Given the lower sampling frequency and duration of our observations at MID4 (every 4 h over 28 h) as compared to previous studies based on in situ mooring observations (e.g., every 15 min over several weeks), we are unable to perform quantitative correlations between the gas concentration data and tidal phase (or light levels). The data presented here provide the first insights into the influence of tidal dynamics and light in western LIS on the distributions of CH_4 and N_2O.

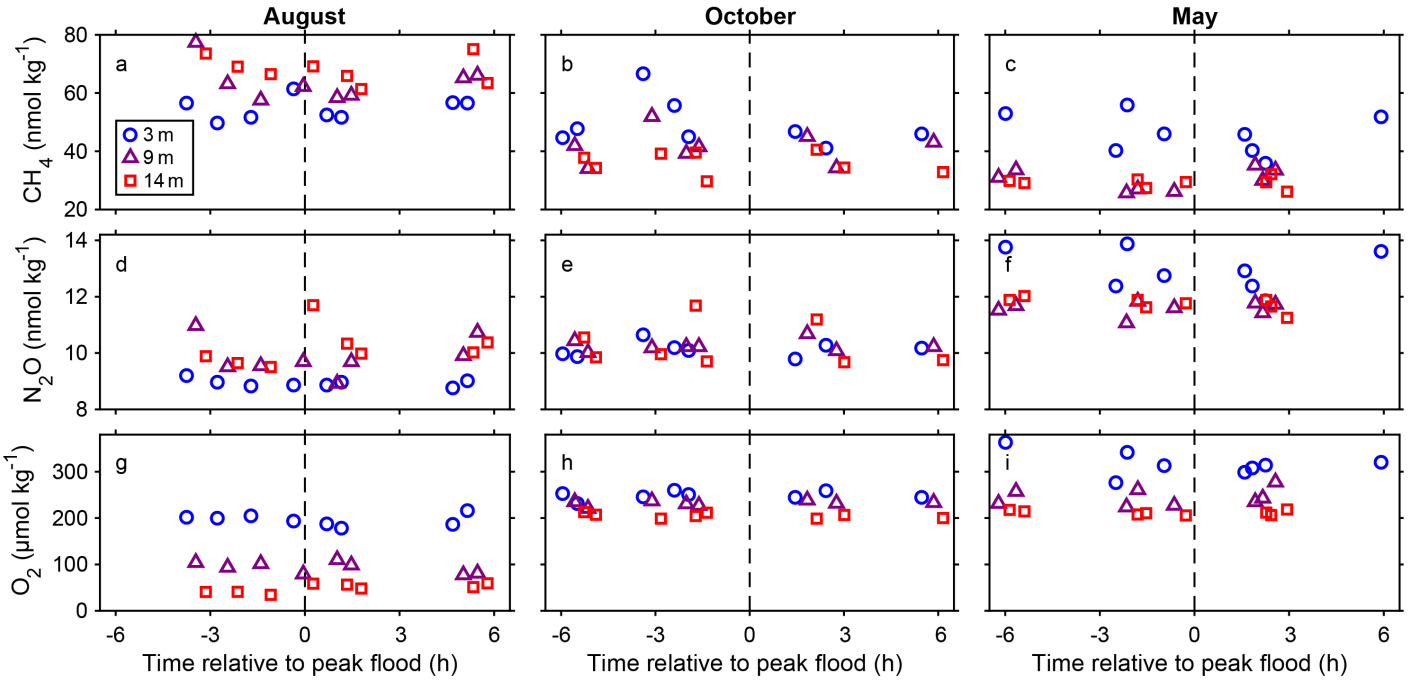

Figure 6. Dissolved gas concentrations at MID4 relative to the timing of peak flood.
Concentrations of CH_4 in nmol kg^{-1} (a–c), N_2O in nmol kg^{-1} (d–f) and O_2 in µmol kg^{-1} (g–i) in August (left), October (center) and May (right column). Blue circles, purple triangles, and red squares represent 3, 9, and 14 m depth, respectively.
Alt Text: Timeseries of dissolved gas concentrations (CH_4, N_2O, and O_2) at station MID4 for each cruise, visualized as a function of time relative to peak flood.

3.4 Sea-air fluxes of CH_4 and N_2O

We calculated sea-air fluxes of CH_4 and N_2O at each station in each season following the 15-day weighting procedure described in section 2.4. Measurements from repeat stations (EXRX and MID4) were averaged to obtain one flux for each station in each month. The surface saturation anomalies, concentrations, and weighted sea-air fluxes of both gases were consistently highest at the westernmost station (EXR1) and followed a general decrease toward the east (Figure 7 and Table 2). Across the seven stations, the mean sea-air CH_4 fluxes (μmol m^{-2} d^{-1}) were 154 in August, 133 in October, and 62 in May, and the mean sea-air N_2O fluxes (μmol m^{-2} d^{-1}) were 2.5 in August, 3.3 in October, and 4.8 in May. Thus, the CH_4 fluxes were highest in August, whereas N_2O fluxes were highest in May.

The gas transfer velocities were similar in all three months. Elevated temperatures (highest in August) and elevated wind speeds (highest in October) both increase the gas transfer velocity. The CH_4 gas transfer velocity averaged 1.4 m d^{-1} in August, 1.6 m d^{-1} in October, and 1.3 m d^{-1} in May, and the N_2O gas transfer velocity averaged 1.4 m d^{-1} in August, 1.5 m d^{-1} in October, and 1.2 m d^{-1} in May. We note that seasonal variability in levels of surfactants and turbidity may influence the gas transfer velocity but these variables are not incorporated into our flux calculation (see section 2.4).

Seasonal variability in the calculated sea-air fluxes was primarily driven by changes in the surface saturation anomaly. For CH_4, August had the highest sea-air flux because the mean CH_4 surface saturation anomaly was 52% higher in August compared to October, even though the gas transfer velocity was 13% lower in August compared to October. For N_2O, the surface N_2O saturation anomaly was highest in May at every station (mean 41%), leading to enhanced fluxes even though the gas transfer velocity was lowest in this month (Table 2).

To estimate annual fluxes, we used the weighted flux data from August, October, and May and applied a linear interpolation at daily frequency over 1 year. The annual mean CH_4 flux was 106 μmol m^{-2} d^{-1} (median 66 μmol m^{-2} d^{-1}) and the annual mean N_2O flux was 3.7 μmol m^{-2} d^{-1} (median 3.2 μmol m^{-2} d^{-1}). This approach has some uncertainty, because we did not collect data during November–April, and we did not utilize wind speed data outside of the 15 days prior to each cruise due to gaps in the mooring wind speed data discussed in section 2.4. Nevertheless, it provides an initial annual estimate for comparison with results from other estuaries worldwide (section 3.8).

Finally, we evaluated the effect of the sampling time on the calculated sea-air fluxes. For station MID4, the relative standard deviation of the weighted CH_4 flux from the 8 time points was 12%, 20%, and 21% in August, October, and May, respectively. The relative standard deviation of the weighted N_2O flux was 14%, 32%, and 28% in August, October, and May, respectively. The variability in sea-air fluxes was primarily driven by concentration changes, as the weighted gas transfer velocity for both gases had a standard deviation of 4% in August and October and 10% in May at MID4. Instantaneous sea-air fluxes showed much stronger variability on sampling time. For example, the relative standard deviation of the instantaneous gas flux at MID4 in May was 135% for CH_4 and 113% for N_2O due to large changes in wind speed during this cruise. This result demonstrates the advantage of using weighted gas fluxes, which incorporate variability in wind speed.

Table 2. Sea-air fluxes, surface concentrations, and surface saturation anomalies of CH_4 and N_2O from all seven stations, calculated using 15-day weighting scheme.

	August		October		May	
Parameter	Median[a]	Mean[b]	Median[a]	Mean[b]	Median[a]	Mean[b]
CH_4 flux ($\mu mol\ m^{-2}\ d^{-1}$)	69 (61, 455)	154 ± 147	72 (40, 287)	133 ± 103	59 (31, 104)	62 ± 25
CH_4 surface concentration ($nmol\ kg^{-1}$)	54 (44, 335)	114 ± 109	50 (28, 185)	86 ± 64	48 (28, 86)	51 ± 21
CH_4 surface saturation anomaly (%)	2200 (1800, 14000)	4700 ± 4600	1800 (900, 6800)	3100 ± 2400	1600 (900, 3000)	1800 ± 700
N_2O flux ($\mu mol\ m^{-2}\ d^{-1}$)	1.9 (1.3, 5.9)	2.5 ± 1.6	2.0 (1.7, 7.5)	3.3 ± 2.2	5.0 (1.9, 8.3)	4.8 ± 2.1
N_2O surface concentration ($nmol\ kg^{-1}$)	8.9 (8.4, 12.1)	9.4 ± 1.3	10.2 (9.9, 13.9)	11.1 ± 1.5	13.1 (10.6, 16.3)	13.1 ± 1.9
N_2O surface saturation anomaly (%)	20 (15, 28)	25 ± 16	14 (12, 54)	23 ± 16	42 (17, 73)	41 ± 18

[a] Values in parentheses represent the first and third quartile, respectively

[b] Uncertainty is the standard deviation. N = 7 in August, 7 in October, and 7 in May.

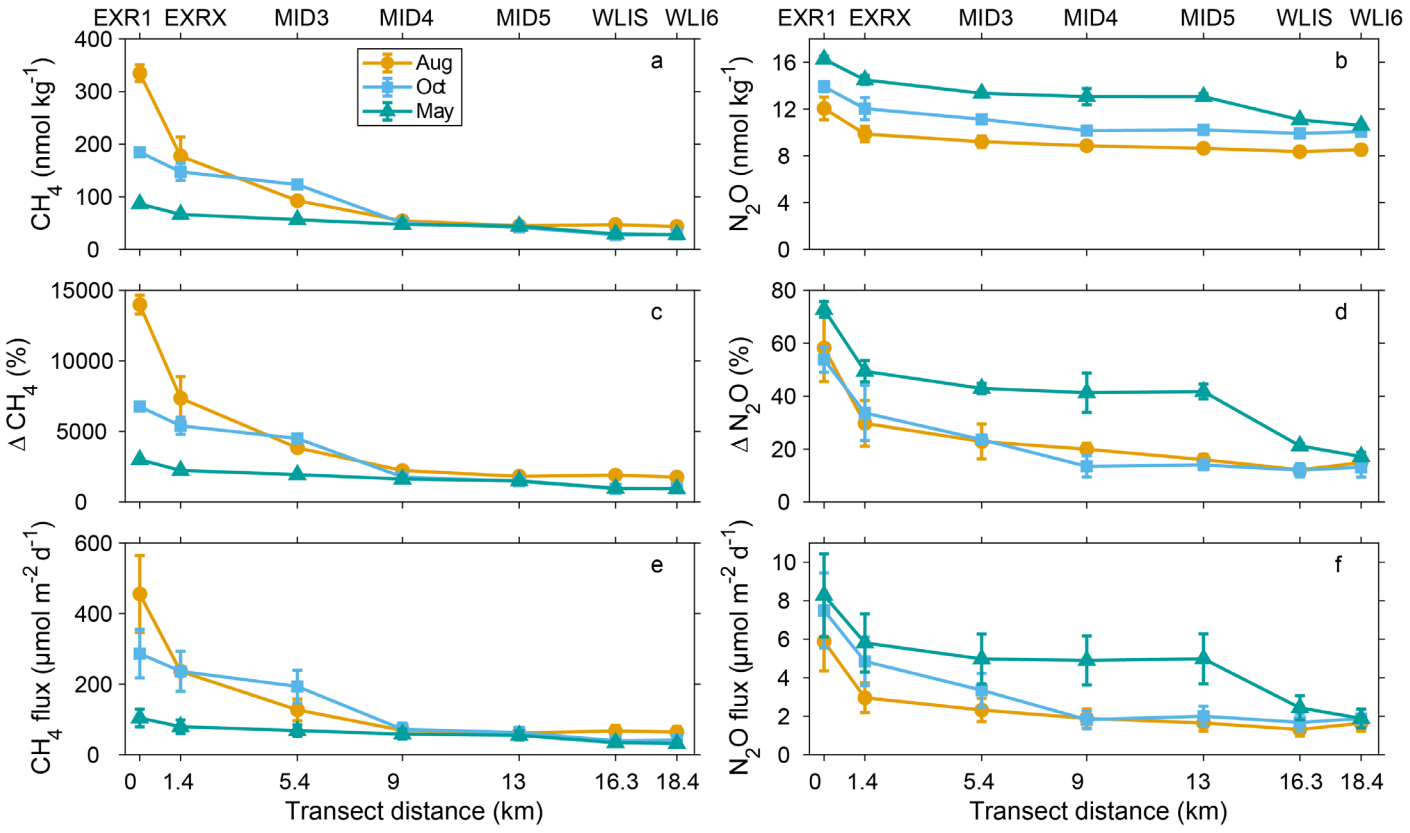

Figure 7. Surface concentrations, surface saturation anomalies and sea-air fluxes of CH_4 and N_2O.
Surface concentrations ($nmol\ kg^{-1}$) of CH_4 (a) and N_2O (b), saturation anomalies (%) of CH_4 (c) and N_2O (d), and sea-air fluxes ($\mu mol\ m^{-2}\ d^{-1}$) of CH_4 (e) and N_2O (f) calculated using a 15-day weighting period for each of the seven stations. The transect distance corresponds to the position of each station along the transect, following Figure 1. Yellow lines and circles, blue lines and squares, and green lines and triangles represent August, October, and May, respectively.

Alt Text: Surface CH_4 and N_2O concentrations, saturation anomalies, and sea-air fluxes. The data show that fluxes and concentrations generally decrease eastward, and that CH_4 fluxes are highest at EXR1 in August whereas N_2O fluxes were highest at EXR1 in May.

3.5 Potential sources and sinks of CH_4 in western LIS

Here we use the observed trends in CH_4 to motivate future studies. We suspect that East River discharge influences surface CH_4 concentrations in western LIS, given the elevated concentrations at the stations closest to the East River where salinity was lowest. Wastewater treatment facilities are significant sources of CH_4, with sources including CH_4 directly released from the wastewater facility, CH_4 emitted from wastewater effluent, and CH_4 production from the degradation of organic matter downstream of the facility (EPA, 2022). Studies of other wastewater facilities indicate that CH_4 concentrations can peak in wastewater effluent and/or downstream of wastewater plants (Alshboul et al., 2016; Jin et al., 2018; Peterse et al., 2024). The East River contains high dissolved organic carbon (DOC) concentrations (around 200 μmol kg^{-1}) which may serve as a substrate for aerobic or anaerobic CH_4 production (Buck et al., 2005). Photodegradation processes following release may increase the bioavailability of DOC (Yin et al., 2021; Yu et al., 2025). Although DOC concentrations are relatively uniform throughout the East River and LIS (Buck et al., 2005), the wastewater effluent-derived DOC present in the East River will have distinct chemical characteristics compared to the terrestrial-derived DOC and natural marine organic matter present farther east in the estuary, and this may affect the production rate of CH_4 from the DOC (Maya-Altamira et al., 2008; Gonsalves et al., 2011; Amaral et al., 2021).

In October and May, CH_4 concentrations were generally higher at the surface than in the subsurface. In August, some stations displayed CH_4 peaks at the surface and subsurface. For example, station EXRX displayed elevated subsurface concentration of CH_4 on August 3 (maximum of 438 nmol kg^{-1} at 16.5 m depth, compared to 203 nmol kg^{-1} at 2.5 m depth). Subsurface peaks could reflect local sedimentary production which is transported to the water column through diffusion and/or ebullition (Bange et al., 2010; Valentine, 2011). Sedimentary effluxes of CH_4, particularly in the form of bubbles, can be strongly influenced by pressure, with lower pressure increasing gas efflux (Maeck et al., 2014; Nylund et al., 2025; Römer et al., 2016). Therefore, changes in tidal stage and overlying water depth may drive effluxes of gases and contribute to some of the spatial variability we observe in near-bottom waters for CH_4. Mazur et al. (2021) performed sediment core incubations and found that stations EXRX and WLIS had on average net negative benthic CH_4 fluxes in summer, though fluxes were widely variable with some cores showing strongly positive fluxes and others negative fluxes. Sediment core incubations cannot account for tidally-driven effluxes. As for N_2O, it is possible that we observed effects of transient CH_4 fluxes from the seafloor interacting with the effects of tidal advection causing transient near-bottom peaks in CH_4.

3.6 Potential sources and sinks of N_2O in western LIS

Here we use the observed gas distributions and published literature on western LIS and the East River to speculate about potential N_2O sources and sinks and motivate future work, which could involve direct measurements of N_2O production and consumption. The highest N_2O concentration and saturation anomaly in our study was observed in the surface waters at station EXR1 in May, rather than in the stratified subsurface hypoxic waters of August, which we initially hypothesized would have the highest concentrations. Our observations of enhanced N_2O concentrations in the fresh water in the far western LIS suggest that either the N_2O is discharged to or produced within the East River, or the substrates that lead to N_2O production are released from the East River and rapidly converted to N_2O within western LIS. Studies in other estuaries and rivers have reported elevated N_2O concentrations in wastewater effluent and/or downstream of some

wastewater treatment plants, though results are highly variable (Burgos et al., 2015; Peterse et al., 2024; Tang, Talbott, et al., 2024).

Water column nitrification rates in oxygenated systems typically increase with reduced competition for NH_4^+ from phytoplankton and decrease with increasing light levels, though different ammonia oxidizing organisms exhibit different light sensitivities (Ward, 2008; Smith et al., 2014; Proctor et al., 2023). In the East River, total ammonia ($NH_4^+ + NH_3$) concentrations are typically above 5 μmol kg^{-1} (and can exceed 40 μmol kg^{-1}), NO_2^- is typically above 2 μmol kg^{-1} (and can exceed 10 μmol kg^{-1}), and NO_3^- is typically above 2 μmol kg^{-1} (and can exceed 30 μmol kg^{-1}) (Gobler et al., 2006; Li et al., 2018). Comparing conditions in the East River and western LIS, salinity is lower, chlorophyll *a* concentrations are lower, and dissolved inorganic nitrogen (DIN) concentrations are higher in the East River (Bowman, 1977; Li et al., 2018; Wallace and Gobler, 2021), making the East River a net exporter of N to western LIS (Buck et al., 2005; Vlahos et al., 2020). These trends suggest that nitrifiers will experience reduced competition for NH_4^+ in the East River compared to western LIS due to the lower phytoplankton biomass and higher DIN. Euphotic zone depths in the East River are on the order of 4 m (reported range 1–8 m), indicating rapid attenuation of light, which is driven by suspended solids rather than phytoplankton biomass and may cause light limitation of phytoplankton growth in some seasons (Li et al., 2018). Somewhat deeper euphotic zone depths of 5–11 m have been reported for LIS (Anderson and Taylor, 2001; Goebel and Kremer, 2007). Given the elevated inorganic N supply and shallow euphotic zone depths in the East River, we expect water column nitrification to be prevalent in this system.

Nitrification has previously been reported in the East River from direct incubation measurements in the early 1970s (Chen et al., 1975). The authors found that nitrification rates increased when the salinity of the incubation water was decreased, suggesting nitrifying microbes in the East River are adapted to the fresh water released from the wastewater plants. Additionally, recent research has proposed that nitrification significantly influences chemical concentrations in the East River (Wallace, 2020; Wallace and Gobler, 2021). Specifically, Wallace and Gobler (2021) estimated aerobic respiration-driven changes in pH and O_2 by collecting diurnal profiles from late afternoon to sunrise and found respiration rates to be lower in the East River than in western LIS. They concluded that aerobic respiration could not fully explain the biogeochemical conditions observed in the East River (low total alkalinity, low O_2, low pH, and high pCO_2) and proposed that ammonification of wastewater-derived organic N followed by nitrification could contribute to these observed conditions. Sedimentary denitrification in the East River is another potential source of N_2O, given the high organic carbon supply. Due to rapid flushing and shallow bottom depths, the East River is not known to reach suboxic conditions in the water column (O'Connor, 1966). However, if denitrification in the East River were the primary driver, we would predict N_2O saturation anomalies to be highest later in the summer following more respiration within the system, rather than in early spring, the start of the productive season.

In western LIS, we observed subsurface peaks in N_2O at the four easternmost stations in August and hypothesize that these trends reflect sedimentary sources, either from denitrification or nitrification. These elevated N_2O concentrations did not display a consistent relationship with O_2. Such a relationship, if observed, could suggest a dominant subsurface source from nitrification below the mixed layer (Nevison et al., 2003). O_2 concentrations were consistently above the threshold for water column denitrification to occur, based on the minimum observed O_2 concentration in this study of 8 μmol kg^{-1} and an O_2 threshold ≤0.01 μmol kg^{-1} for denitrification (Zakem and Follows, 2017; Zakem et al., 2020). However, anoxic microenvironments within organisms, aggregates, and suspended/sinking particles may have provided sites for anaerobic metabolic processes to occur (Klawonn et al., 2015; Bianchi et al., 2018; Wan, Sheng, Dai, et al., 2023; Wan, Sheng, Liu, et al., 2023). Mazur et al. (2021) conducted sediment core incubations in western LIS and found sediments were on average a small net source of N_2O (mean 8.6 nmol N_2O m^{-2} h^{-1}) but sediment-water fluxes varied widely (range −32 to 68 nmol N_2O m^{-2} h^{-1}). Variability in sedimentary N_2O fluxes is consistent with our

observation that stations with similar bottom-water O_2 concentrations had variable N_2O concentrations and vertical gradients in N_2O.

3.7 Role of CH_4 and N_2O in western LIS C and N budgets and global warming potential of emissions

We assessed the contribution of CH_4 and N_2O to the overall C and N budgets for LIS. CH_4 concentrations in our study were ≤0.5 μmol kg^{-1}, whereas dissolved organic carbon concentrations typically exceed 100 μmol kg^{-1} and dissolved inorganic carbon concentrations typically exceed 1600 μmol kg^{-1} (Vlahos and Whitney, 2017; Barrett et al., 2024). Dissolved N_2O concentrations did not exceed 0.016 μmol kg^{-1} in our study, whereas total inorganic N concentrations (excluding N_2 gas, which is not bioavailable to most organisms) in western LIS typically exceed 14 μmol kg^{-1} (Vlahos et al., 2020). Therefore, CH_4 and N_2O are not significant components of the total C and N budgets in western LIS.

We converted the CH_4 and N_2O fluxes to units of CO_2-equivalents (CO_2e) and compared these values to estimated fluxes of CO_2, the anthropogenic greenhouse gas that is the biggest contributor to global warming (Forster et al., 2021). The global warming potential (GWP) quantifies how much heat a greenhouse gas traps in the atmosphere over a specific time relative to the same mass of CO_2. We use a 100-year global warming potential (GWP-100) of 27 for CH_4 and 273 for N_2O (Forster et al., 2021). Because contemporaneous measurements of CO_2 were not collected, we use surface pCO_2 measurements by Wallace and Gobler (2021) collected in 2014 at stations MID4 and EXCR (named B3 and A4, respectively, in that study) to provide an initial and approximate evaluation of the relative importance of CO_2, CH_4, and N_2O emissions from western LIS. Using the wind speeds measured in 2023–2024 and the pCO_2 concentrations from June–September 2014 (ranging from 600 to 1300 μatm), the estimated CO_2 fluxes averaged 0.8 g CO_2 m^{-2} d^{-1} at MID4 and 2 g CO_2 m^{-2} d^{-1} at EXCR. Using our data from August, October, and May, we calculated an average CH_4 flux of 0.03 g CO_2e m^{-2} d^{-1} at MID4 and 0.08 g CO_2e m^{-2} d^{-1} at EXCR, and an average N_2O flux of 0.03 g CO_2e m^{-2} d^{-1} at MID4 and 0.05 g CO_2e m^{-2} d^{-1} at EXCR. Therefore, N_2O and CH_4 emissions from western LIS each likely generate ≤5% of the radiative forcing caused by CO_2 over 100 years. These results could be further refined through future studies measuring all three gases simultaneously.

3.8 Western LIS sea-air CH_4 and N_2O fluxes and concentrations in the global context

In general, the CH_4 and N_2O fluxes we estimate for western LIS fall within the range of prior studies which have concluded that estuaries play a small role in global CH_4 and N_2O budgets. Globally, CH_4 and N_2O concentrations and sea-air fluxes from estuarine systems are highly variable and have a positively skewed distribution, making global upscaling highly sensitive to the dataset and model used (Rosentreter et al., 2021; Zheng et al., 2022).

The sea-air CH_4 fluxes we estimate for western LIS (annual mean of 106 μmol m^{-2} d^{-1} and median of 66 μmol m^{-2} d^{-1}) are comparable to a recent global metanalysis by Rosentreter et al. (2021) which reported a mean estuarine CH_4 flux of 151 μmol m^{-2} d^{-1} and a median of 38 μmol m^{-2} d^{-1} (N = 53 sites), and a global metanalysis by Zheng et al. (2022) which reported a mean diffusive estuarine CH_4 flux of 780 μmol m^{-2} d^{-1} and a median of 120 μmol m^{-2} d^{-1} (N = 91 sites). The estuarine concentrations reported in Zheng et al. (2022) had a mean of 230 nmol kg^{-1} and a median of 110 nmol kg^{-1}—comparable to our surface measurements in western

LIS (annual mean of 78 nmol kg^{-1} and median of 50 nmol kg^{-1}). The maximum estuarine concentration reported in the metanalysis was 2300 nmol kg^{-1} and the maximum diffusive flux was 27,000 μmol m^{-2} d^{-1} (Zheng et al., 2022). The fluxes we report are for diffusive processes only. Ebullitive fluxes can be a significant contributor to CH_4 emissions in aquatic systems <5 m deep, but in deeper systems such as western LIS, diffusive fluxes dominate as the vast majority of bubbles released from the sediment will dissolve before reaching the surface (Joyce and Jewell, 2003; West et al., 2016). Globally, estuaries are thought to contribute emissions of 1–6 Tg CH_4 y^{-1} based on mean fluxes from global data compilations (Rosentreter et al., 2021; Zheng et al., 2022), which is ≤1% of global CH_4 emissions from both natural and anthropogenic sources, currently estimated at 540–865 Tg CH_4 y^{-1} (Saunois et al., 2025).

Our N_2O fluxes, estimated to have an annual mean of 3.7 μmol m^{-2} d^{-1} and median of 3.2 μmol m^{-2} d^{-1} are comparable to, though on the low end, of published typical ranges for estuaries. For example, the global metanalysis of Zheng et al. (2022) reported a mean estuarine N_2O water-air flux of 19 μmol m^{-2} d^{-1} and a median of 6 μmol m^{-2} d^{-1} (minimum −7 μmol m^{-2} d^{-1}, maximum 177 μmol m^{-2} d^{-1}) based on 83 studies. Their mean estuarine N_2O concentration of 32 nmol kg^{-1} and median of 15 nmol kg^{-1} (minimum 4 nmol kg^{-1}, maximum 210 nmol kg^{-1}) are also comparable, though trending somewhat higher than the surface concentrations we observed (annual mean of 11.5 nmol kg^{-1} and median of 11.1 nmol kg^{-1}). Globally, N_2O emissions from inland waters, estuaries, and coastal vegetation were estimated for the year 2020 as 0.1 (range 0–0.2) Tg N y^{-1} (Tian et al., 2024), whereas the study of Zheng et al. (2022) estimated a higher flux of 0.25 Tg N y^{-1} from estuaries alone. Both values are small in comparison to total net N_2O emissions from all anthropogenic and natural sources, estimated at 18.5 Tg N y^{-1} (range 10.6–27.0 Tg N y^{-1}) from bottom-up approaches that incorporate flux measurements, data-based nitrogen inventories, and models (Tian et al., 2024).

4. Conclusions

We have obtained the first measurements of CH_4 and N_2O in western LIS, a eutrophic urban estuary, in summer, fall, and spring. Although both gases can be generated under processes associated with organic matter remineralization and low-oxygen conditions in subsurface waters, we found that both CH_4 and N_2O often displayed higher concentrations at the surface compared to the subsurface. Both gases showed an along-estuary gradient in the near-surface, and concentrations in the upper 10 m were highest at the westernmost station (closest to the East River and New York City) in all three seasons. Conversely, near-surface O_2 concentrations were typically lowest at the westernmost stations and decreased eastward. Hypoxic conditions in August were associated with elevated CH_4 concentrations and sea-air fluxes. However, N_2O concentrations and fluxes were highest in May, indicating that biogeochemical processes associated with seasonal hypoxia are not the primary driver of N_2O dynamics in western LIS. Repeat measurements at station MID4 suggested that sub-daily variability in O_2, CH_4, and N_2O concentrations could not be correlated solely to daily changes in light or tidal phase. Sea-air fluxes of CH_4 and N_2O were comparable with other estuaries worldwide.

Our dataset suggests there is a persistent source of fresh surface water elevated in CH_4 and N_2O (or substrates that support production of these gases) to western LIS which enhances surface concentrations and sea-air fluxes in this region. Future work could focus on mapping the distributions of these gases in the East River and in proximity to wastewater inputs. To determine production and consumption mechanisms and rates, incubation experiments could be combined with metagenomic analyses (Karl et al., 2008; Uhlig and Loose, 2017; Euler et al., 2020; Bourbonnais et al., 2021; Rasmussen and Francis, 2022). Ongoing changes in western LIS include reductions in nutrient loading, increased water temperatures, reductions in O_2 solubility,

and ocean acidification (Wallace and Gobler, 2021; Whitney and Vlahos, 2021). Continued monitoring along with targeted experiments evaluating the impacts of multiple stressors would improve predictions of how projected future changes will influence greenhouse gas emissions (Tang, Da, et al., 2024).

Data accessibility statement: The following datasets were generated.
Manning, CCM; Payyambally, A; Mottram, J; Ward, K (2026): Methane and nitrous oxide dissolved gas concentrations from western Long Island Sound [dataset].
PANGAEA, https://doi.org/10.1594/PANGAEA.987944

Manning, CCM; Payyambally, A; Mottram, J; Ward, K (2026): Methane and nitrous oxide sea-air fluxes from western Long Island Sound [dataset]. PANGAEA, https://doi.org/10.1594/PANGAEA.987952

Contributions:
Contributed to conception and design: CM, AP, KW
Contributed to acquisition of data: CM, AP, JM, KW
Contributed to analysis and interpretation of data: CM
Drafted and/or revised the article: CM, AP, JM, KW
Approved the submitted version for publication: CM, AP, JM, KW

Acknowledgements:
We thank the captain, crew, and science teams on the trips for their support of the research. We thank Julie Granger for providing feedback on a draft of the manuscript, and Mingxi Yang, Lisa Miller, and an anonymous reviewer for constructive reviews that improved the manuscript.

Funding: Ship time on the *R/V Connecticut* was funded through project R/CMC-20/CTNY funded under award LI-96196201, US Environmental Protection Agency, to the Sponsored Program Services of the University of Connecticut on behalf of Connecticut Sea Grant, and in collaboration with NYSG. The statements, findings, conclusions, views, and recommendations are those of the authors and do not necessarily reflect the views of any of those organizations. Acquisition of data at NOAA mooring 44022 used in this study was supported through the Long Island Sound Integrated Coastal Observatory (LISICOS) which is funded by NOAA. Additional funding for the research was provided by the University of Connecticut to CM.

Competing interests:
The authors declare no competing interests.

References

Abril G, Commarieu M-V, Sottolichio A, Bretel P, Guérin F. 2009. Turbidity limits gas exchange in a large macrotidal estuary. *Estuarine, Coastal and Shelf Science* **83**(3): 342–348. doi: 10.1016/j.ecss.2009.03.006

Alshboul Z, Encinas-Fernández J, Hofmann H, Lorke A. 2016. Export of Dissolved Methane and Carbon Dioxide with Effluents from Municipal Wastewater Treatment Plants. *Environ Sci Technol* **50**(11): 5555–5563. American Chemical Society. doi: 10.1021/acs.est.5b04923

Amaral V, Ortega T, Romera-Castillo C, Forja J. 2021. Linkages between greenhouse gases (CO2, CH4, and N2O) and dissolved organic matter composition in a shallow estuary. *Science of The Total Environment* **788**: 147863. doi: 10.1016/j.scitotenv.2021.147863

Anderson TH, Taylor GT. 2001. Nutrient pulses, plankton blooms, and seasonal hypoxia in western Long Island Sound. *Estuaries* **24**(2): 228–243. doi: 10.2307/1352947

Bange HW, Freing A, Kock A, Löscher CR. 2010. Marine Pathways to Nitrous Oxide. In: *Nitrous Oxide and Climate Change*1st ed. Routledge. p. 36–62. Available at https://doi.org/10.4324/9781849775113.

Barrett LJ, Vlahos P, McGuinness MA, Whitney MM, Vaudrey JMP. 2024. Droughts and deluges: changes in river discharge and the carbonate chemistry of an urbanized temperate estuary. *Front Mar Sci* **11**. Frontiers. doi: 10.3389/fmars.2024.1398087

Bennett DC, O'Donnell J, Bohlen WF, Houk A. 2010. Tides and Overtides in Long Island Sound. *j mar res* **68**(1): 1–35. doi: 10.1357/002224010793079031

Bianchi D, Weber TS, Kiko R, Deutsch C. 2018. Global niche of marine anaerobic metabolisms expanded by particle microenvironments. *Nature Geosci* **11**(4): 263–268. Nature Publishing Group. doi: 10.1038/s41561-018-0081-0

Bittig HC, Körtzinger A, Neill C, van Ooijen E, Plant JN, Hahn J, Johnson KS, Yang B, Emerson SR. 2018. Oxygen Optode Sensors: Principle, Characterization, Calibration, and Application in the Ocean. *Front Mar Sci* **4**. Frontiers. doi: 10.3389/fmars.2017.00429

Blumberg AF, Pritchard DW. 1997. Estimates of the transport through the East River, New York. *Journal of Geophysical Research: Oceans* **102**(C3): 5685–5703. doi: 10.1029/96JC03416

Borges AV, Delille B, Schiettecatte L-S, Gazeau F, Abril G, Frankignoulle M. 2004. Gas transfer velocities of CO2 in three European estuaries (Randers Fjord, Scheldt, and Thames). *Limnology and Oceanography* **49**(5): 1630–1641. doi: 10.4319/lo.2004.49.5.1630

Bourbonnais A, Frey C, Sun X, Bristow LA, Jayakumar A, Ostrom NE, Casciotti KL, Ward BB. 2021. Protocols for Assessing Transformation Rates of Nitrous Oxide in the Water Column. *Front Mar Sci* **8**. Frontiers. doi: 10.3389/fmars.2021.611937

Bowman MJ. 1977. Nutrient distributions and transport in Long Island Sound. *Estuarine and Coastal Marine Science* **5**(4): 531–548. doi: 10.1016/0302-3524(77)90100-1

Buck NJ, Gobler CJ, Sañudo-Wilhelmy SA. 2005. Dissolved Trace Element Concentrations in the East River−Long Island Sound System: Relative Importance of Autochthonous versus Allochthonous Sources. *Environ Sci Technol* **39**(10): 3528–3537. American Chemical Society. doi: 10.1021/es048860t

Burgos M, Sierra A, Ortega T, Forja JM. 2015. Anthropogenic effects on greenhouse gas (CH4 and N2O) emissions in the Guadalete River Estuary (SW Spain). *Science of The Total Environment* **503–504**: 179–189. doi: 10.1016/j.scitotenv.2014.06.038

Capelle DW, Hallam SJ, Tortell PD. 2019. Time-series CH4 measurements from Saanich Inlet, BC, a seasonally anoxic fjord. *Marine Chemistry* **215**: 103664. doi: 10.1016/j.marchem.2019.103664

Capelle DW, Tortell PD. 2016. Factors controlling methane and nitrous-oxide variability in the southern British Columbia coastal upwelling system. **179**(C): 56–67. doi: 10.1016/j.marchem.2016.01.011

Chen M, Canelli E, Fuhs GW. 1975. Effects of Salinity on Nitrification in the East River. *Journal (Water Pollution Control Federation)* **47**(10): 2474–2481. Water Environment Federation.

Damm E, Thoms S, Beszczynska-Möller A, Nöthig EM, Kattner G. 2015. Methane excess production in oxygen-rich polar water and a model of cellular conditions for this paradox. *Polar Science* **9**(3): 327–334. doi: 10.1016/j.polar.2015.05.001

Diaz RJ, Rosenberg R. 2008. Spreading Dead Zones and Consequences for Marine Ecosystems. *Science* **321**(5891): 926–929. American Association for the Advancement of Science. doi: 10.1126/science.1156401

Dlugokencky EJ, Crotwell AM, Mund JW, Crotwell MJ, Thoning KW. 2020a. Atmospheric Methane Dry Air Mole Fractions from the NOAA GML Carbon Cycle Cooperative Global Air Sampling Network, 1983-2019, Version: 2020-07. Available at https://doi.org/10.15138/VNCZ-M766.

Dlugokencky EJ, Crotwell AM, Mund JW, Crotwell MJ, Thoning KW. 2020b. Atmospheric Nitrous Oxide Dry Air Mole Fractions from the NOAA GML Carbon Cycle Cooperative Global Air Sampling Network, 1997-2019, Version: 2020-07. Available at https://doi.org/10.15138/53g1-x417.

Dlugokencky EJ, Steele LP, Lang PM, Masarie KA. 1994. The growth rate and distribution of atmospheric methane. *Journal of Geophysical Research: Atmospheres* **99**(D8): 17021–17043. doi: https://doi.org/10.1029/94JD01245

Duvall MS, Hagy JD, Ammerman JW, Tedesco MA. 2024. High-frequency Dissolved Oxygen Dynamics in an Urban Estuary, the Long Island Sound. *Estuaries and Coasts* **47**(2): 415–430. doi: 10.1007/s12237-023-01278-8

EPA. 2022. Inventory of U.S. Greenhouse Gas Emissions and Sinks: 1990-2020. U.S. Environmental Protection Agency, EPA 430-R-22-003. Available at https://www.epa.gov/system/files/documents/2022-04/us-ghg-inventory-2022-main-text.pdf. Accessed 2025 Sept 2.

Euler S, Jeffrey LC, Maher DT, Mackenzie D, Tait DR. 2020. Shifts in methanogenic archaea communities and methane dynamics along a subtropical estuarine land use gradient. *PLOS ONE* **15**(11): e0242339. Public Library of Science. doi: 10.1371/journal.pone.0242339

Fazi S, Amalfitano S, Venturi S, Pacini N, Vazquez E, Olaka LA, Tassi F, Crognale S, Herzsprung P, Lechtenfeld OJ, et al. 2021. High concentrations of dissolved biogenic methane associated with cyanobacterial blooms in East African lake surface water. *Commun Biol* **4**(1): 845. Nature Publishing Group. doi: 10.1038/s42003-021-02365-x

Forster P, Storelvmo T, Armour K. 2021. Chapter 7: The Earth's Energy Budget, Climate Feedbacks, and Climate Sensitivity. In: *Climate Change 2021 – The Physical Science Basis: Working Group I Contribution to the Sixth Assessment Report of the Intergovernmental Panel on Climate Change*1st ed. Cambridge University Press. p. 923–1054. Available at https://www.ipcc.ch/report/ar6/wg1/downloads/report/IPCC_AR6_WGI_Chapter07.pdf. Accessed 2025 Sept 1.

Gay PS, O'Donnell J, Edwards CA. 2004. Exchange between Long Island Sound and adjacent waters. *Journal of Geophysical Research: Oceans* **109**(C6). doi: 10.1029/2004JC002319

GEBCO Compilation Group. 2024. GEBCO 2024 Grid. doi: https://dx.doi.org/10.5285/1c44ce99-0a0d-5f4f-e063-7086abc0ea0f

Gobler CJ, Buck NJ, Sieracki ME, Sañudo-Wilhelmy SA. 2006. Nitrogen and silicon limitation of phytoplankton communities across an urban estuary: The East River-Long Island Sound system. *Estuarine, Coastal and Shelf Science* **68**(1): 127–138. doi: 10.1016/j.ecss.2006.02.001

Goebel N, Kremer J. 2007. Temporal and spatial variability of photosynthetic parameters and community respiration in Long Island Sound. *Mar Ecol Prog Ser* **329**: 23–42. doi: 10.3354/meps329023

Gonsalves M-J, Fernandes CEG, Fernandes SO, Kirchman DL, Bharathi PAL. 2011. Effects of composition of labile organic matter on biogenic production of methane in the coastal sediments of the Arabian Sea. *Environ Monit Assess* **182**(1): 385–395. doi: 10.1007/s10661-011-1883-3

Hall BD, Dutton GS, Elkins JW. 2007. The NOAA nitrous oxide standard scale for atmospheric observations. *Journal of Geophysical Research (Atmospheres)* **112**: 09305.

Hall N, Wong WW, Lappan R, Ricci F, Jeppe KJ, Glud RN, Kawaichi S, Rotaru A-E, Greening C, Cook PLM. 2025 Aug 7. Coastal methane emissions driven by aerotolerant methanogens using seaweed and seagrass metabolites. *Nat Geosci*: 1–8. Nature Publishing Group. doi: 10.1038/s41561-025-01768-3

Harley JF, Carvalho L, Dudley B, Heal KV, Rees RM, Skiba U. 2015. Spatial and seasonal fluxes of the greenhouse gases N2O, CO2 and CH4 in a UK macrotidal estuary. *Estuarine, Coastal and Shelf Science* **153**: 62–73. doi: 10.1016/j.ecss.2014.12.004

Hayduk W, Laudie H. 1974. Prediction of diffusion coefficients for nonelectrolytes in dilute aqueous solutions. *AIChE Journal* **20**(3): 611–615. doi: 10.1002/aic.690200329

Ho DT, Schlosser P, Orton PM. 2011. On Factors Controlling Air–Water Gas Exchange in a Large Tidal River. *Estuaries and Coasts* **34**(6): 1103–1116. doi: 10.1007/s12237-011-9396-4

Howarth R, Chan F, Conley DJ, Garnier J, Doney SC, Marino R, Billen G. 2011. Coupled biogeochemical cycles: eutrophication and hypoxia in temperate estuaries and coastal marine ecosystems. *Frontiers in Ecology and the Environment* **9**(1): 18–26. doi: 10.1890/100008

Hsu SA, Meindl EA, Gilhousen DB. 1994. Determining the power-law wind-profile exponent under near-neutral stability conditions at sea. *Journal of Applied …* **33**(6): 757–765. doi: 10.1175/1520-0450(1994)033<0757:DTPLWP>2.0.CO;2

Irby ID, Friedrichs MAM, Da F, Hinson KE. 2018. The competing impacts of climate change and nutrient reductions on dissolved oxygen in Chesapeake Bay. *Biogeosciences* **15**(9): 2649–2668. Copernicus GmbH. doi: 10.5194/bg-15-2649-2018

Izett RW, Fennel K, Stoer AC, Nicholson DP. 2024. Reviews and syntheses: expanding the global coverage of gross primary production and net community production measurements using Biogeochemical-Argo floats. *Biogeosciences* **21**(1): 13–47. Copernicus GmbH. doi: 10.5194/bg-21-13-2024

Jähne B, Heinz G, Dietrich W. 1987. Measurement of the Diffusion Coefficients of Sparingly Soluble Gases in Water. *J Geophys Res* **92**(C10): 10767–10776. doi: 10.1029/JC092iC10p10767

Jin H, Yoon TK, Begum MS, Lee E-J, Oh N-H, Kang N, Park J-H. 2018. Longitudinal discontinuities in riverine greenhouse gas dynamics generated by dams and urban wastewater. *Biogeosciences* **15**(20): 6349–6369. Copernicus GmbH. doi: 10.5194/bg-15-6349-2018

Joyce J, Jewell PW. 2003. Physical controls on methane ebullition from reservoirs and lakes. *Environmental & Engineering Geoscience* **9**(2): 167–178.

Karl DM, Beversdorf L, Björkman KM, Church MJ, Martinez A, Delong EF. 2008. Aerobic production of methane in the sea. *Nature Geosci* **1**(7): 473–478. doi: 10.1038/ngeo234

Klawonn I, Bonaglia S, Brüchert V, Ploug H. 2015. Aerobic and anaerobic nitrogen transformation processes in N2-fixing cyanobacterial aggregates. *ISME J* **9**(6): 1456–1466. doi: 10.1038/ismej.2014.232

Kock A, Arévalo-Martínez DL, Löscher CR, Bange HW. 2016. Extreme N2O accumulation in the coastal oxygen minimum zone off Peru. *Biogeosciences* **13**(3): 827–840. doi: 10.5194/bg-13-827-2016

Lan X, Nisbet EG, Dlugokencky EJ, Michel SE. 2021. What do we know about the global methane budget? Results from four decades of atmospheric CH4 observations and the way forward. *Philosophical Transactions of the Royal Society A: Mathematical, Physical and Engineering Sciences* **379**(2210): 20200440. Royal Society. doi: 10.1098/rsta.2020.0440

Langdon C. 2010. Determination of dissolved oxygen in seawater by Winkler titration using the amperometric technique. *The GO-SHIP Repeat Hydrography Manual: A Collection of Expert Repots and Guidelines* **IOCCP Report No. 14, ICPO Publication Series No. 134**(Version 1): 18. doi: https://doi.org/10.25607/OBP-1350

Lee YJ, Lwiza K. 2005. Interannual variability of temperature and salinity in shallow water: Long Island Sound, New York. *Journal of Geophysical Research: Oceans* **110**(C9). doi: 10.1029/2004JC002507

Lee YJ, Lwiza KMM. 2008. Characteristics of bottom dissolved oxygen in Long Island Sound, New York. *Estuarine, Coastal and Shelf Science* **76**(2): 187–200. doi: 10.1016/j.ecss.2007.07.001

Leon-Palmero E, Morales-Baquero R, Thamdrup B, Löscher C, Reche I. 2025. Sunlight drives the abiotic formation of nitrous oxide in fresh and marine waters. *Science* **387**(6739): 1198–1203. doi: 10.1126/science.adq0302

Li Y, Fichot CG, Geng L, Scarratt MG, Xie H. 2020. The Contribution of Methane Photoproduction to the Oceanic Methane Paradox. *Geophysical Research Letters* **47**(14): e2020GL088362. doi: https://doi.org/10.1029/2020GL088362

Li Y, Meseck SL, Dixon MS, Wikfors GH. 2018. The East River tidal strait, New York City, New York, a high-nutrient, low-chlorophyll coastal system. *Int Aquat Res* **10**(1): 65–77. doi: 10.1007/s40071-018-0189-2

Maeck A, Hofmann H, Lorke A. 2014. Pumping methane out of aquatic sediments – ebullition forcing mechanisms in an impounded river. *Biogeosciences* **11**(11): 2925–2938. Copernicus GmbH. doi: 10.5194/bg-11-2925-2014

Magen C, Lapham LL, Pohlman JW, Marshall K, Bosman S, Casso M, Chanton JP. 2014. A simple headspace equilibration method for measuring dissolved methane. *Limnology and Oceanography: Methods* **12**(9): 637–650. doi: 10.4319/lom.2014.12.637

Manning CCM, Nicholson DP. 2026. dnicholson/gas_toolbox: MATLAB code for calculating gas fluxes. doi: https://doi.org/10.5281/zenodo.6126684

Manning CCM, Payyambally A, Mottram J, Ward K. 2026a. Methane and nitrous oxide dissolved gas concentrations from western Long Island Sound [dataset]. PANGAEA. doi: https://doi.org/10.1594/PANGAEA.987944

Manning CCM, Payyambally A, Mottram J, Ward K. 2026b. Methane and nitrous oxide sea-air fluxes from western Long Island Sound [dataset]. PANGAEA. doi: https://doi.org/10.1594/PANGAEA.987952

Manning CCM, Zheng Z, Fenwick L, McCulloch RD, Damm E, Izett RW, Williams WJ, Zimmermann S, Vagle S, Tortell PD. 2022. Interannual Variability in Methane and Nitrous Oxide Concentrations and Sea-Air Fluxes Across the North American Arctic Ocean (2015–2019). *Global Biogeochemical Cycles* **36**(4): e2021GB007185. doi: 10.1029/2021GB007185

Mao S-H, Zhang H-H, Zhuang G-C, Li X-J, Liu Q, Zhou Z, Wang W-L, Li C-Y, Lu K-Y, Liu X-T, et al. 2022. Aerobic oxidation of methane significantly reduces global diffusive methane emissions from shallow marine waters. *Nat Commun* **13**(1): 7309. Nature Publishing Group. doi: 10.1038/s41467-022-35082-y

Martens CS, Berner RA. 1974. Methane Production in the Interstitial Waters of Sulfate-Depleted Marine Sediments. *Science* **185**(4157): 1167–1169. American Association for the Advancement of Science. doi: 10.1126/science.185.4157.1167

Martens CS, Berner RA. 1977. Interstitial water chemistry of anoxic Long Island Sound sediments. 1. Dissolved gases1. *Limnology and Oceanography* **22**(1): 10–25. doi: 10.4319/lo.1977.22.1.0010

Martini M, Butman B, Mickelson MJ. 2007 Nov 1. Long-Term Performance of Aanderaa Optodes and Sea-Bird SBE-43 Dissolved-Oxygen Sensors Bottom Mounted at 32 m in Massachusetts Bay. , in press. doi: 10.1175/JTECH2078.1

Mau S, Blees J, Helmke E, Niemann H, Damm E. 2013. Vertical distribution of methane oxidation and methanotrophic response to elevated methane concentrations in stratified waters of the Arctic fjord Storfjorden (Svalbard, Norway). *Biogeosciences* **10**(10): 6267–6278. doi: 10.5194/bg-10-6267-2013

Maya-Altamira L, Baun A, Angelidaki I, Schmidt JE. 2008. Influence of wastewater characteristics on methane potential in food-processing industry wastewaters. *Water Research* **42**(8): 2195–2203. doi: 10.1016/j.watres.2007.11.033

Mazur CI, Al-Haj AN, Ray NE, Sanchez-Viruet I, Fulweiler RW. 2021. Low denitrification rates and variable benthic nutrient fluxes characterize Long Island Sound sediments. *Biogeochemistry* **154**(1): 37–62. doi: 10.1007/s10533-021-00795-7

McCardell G, O'Donnell J, Souza AJ, Palmer MR. 2016. Internal tides and tidal cycles of vertical mixing in western Long Island Sound. *Journal of Geophysical Research: Oceans* **121**(2): 1063–1084. doi: 10.1002/2015JC010796

Naqvi SWA, Bange HW, Farías L, Monteiro PMS, Scranton MI, Zhang J. 2010. Marine hypoxia/anoxia as a source of CH_4 and N_2O. *Biogeosciences* **7**(7): 2159–2190. doi: 10.5194/bg-7-2159-2010

Nevison C, Butler JH, Elkins JW. 2003. Global distribution of N_2O and the ΔN_2O-AOU yield in the subsurface ocean. *Global Biogeochemical Cycles* **17**(4). doi: 10.1029/2003GB002068

Nicholson DP, Wilson ST, Doney SC, Karl DM. 2015. Quantifying subtropical North Pacific gyre mixed layer primary productivity from Seaglider observations of diel oxygen cycles. *Geophysical Research Letters* **42**(10): 4032–4039. doi: https://doi.org/10.1002/2015GL063065

NOAA. 2025. NOAA. NOAA Current Predictions - Current Predictions. Available at https://tidesandcurrents.noaa.gov/noaacurrents/predictions.html?id=LIS1035_12. Accessed 2025 Oct 4.

NYCDEP. 2025. NYCDEP. Wastewater Treatment Plants - New York City Department of Environmental Protection. Available at https://www.nyc.gov/site/dep/water/wastewater-treatment-plants.page. Accessed 2025 Oct 4.

Nylund AT, Mellqvist J, Conde V, Salo K, Bensow R, Arneborg L, Jalkanen J-P, Tengberg A, Hassellöv I-M. 2025. Coastal methane emissions triggered by ship passages. *Commun Earth Environ* **6**(1): 380. Nature Publishing Group. doi: 10.1038/s43247-025-02344-8

O'Connor DJ. 1966. An Analysis of the Dissolved Oxygen Distribution in the East River. *Journal (Water Pollution Control Federation)* **38**(11): 1813–1830. Water Environment Federation.

O'Donnell J, Dam HG, Bohlen WF, Fitzgerald W, Gay PS, Houk AE, Cohen DC, Howard-Strobel MM. 2008. Intermittent ventilation in the hypoxic zone of western Long Island Sound during the summer of 2004. *Journal of Geophysical Research: Oceans* **113**(C9). doi: 10.1029/2007JC004716

O'Donnell J, Wilson RE, Lwiza K, Whitney M, Bohlen WF, Codiga D, Fribance DB, Fake T, Bowman M, Varekamp J. 2014. The Physical Oceanography of Long Island Sound. In: Latimer JS, Tedesco MA, Swanson RL, Yarish C, Stacey PE, Garza C, editors. *Long Island Sound*. New York, NY: Springer New York. p. 79–158. doi: 10.1007/978-1-4614-6126-5_3

Parker CA, O'Reilly JE. 1991. Oxygen Depletion in Long Island Sound: A Historical Perspective. *Estuaries* **14**(3): 248–264.

de la Paz M, Ferrón S, Borges AV, Upstill-Goddard RC. 2021. Quantification of dissolved methane and nitrous oxide via headspace equilibrium. Available at https://orbi.uliege.be/bitstream/2268/253977/1/SOP5-OCB-Report-v6c.pdf. Accessed 2025 Aug 2.

Perez-Coronel E, Beman JM. 2022. Multiple sources of aerobic methane production in aquatic ecosystems include bacterial photosynthesis. *Nat Commun* **13**(1): 6454. Nature Publishing Group. doi: 10.1038/s41467-022-34105-y

Peterse IF, Hendriks L, Weideveld STJ, Smolders AJP, Lamers LPM, Lücker S, Veraart AJ. 2024. Wastewater-effluent discharge and incomplete denitrification drive riverine CO2, CH4 and N2O emissions. *Science of The Total Environment* **951**: 175797. doi: 10.1016/j.scitotenv.2024.175797

Proctor C, Coupel P, Casciotti K, Tremblay J-E, Zakem E, Arrigo KR, Mills MM. 2023. Light, ammonium, pH, and phytoplankton competition as environmental factors controlling nitrification. *Limnology and Oceanography* **68**(7): 1490–1503. doi: 10.1002/lno.12359

Rasmussen AN, Francis CA. 2022. Genome-Resolved Metagenomic Insights into Massive Seasonal Ammonia-Oxidizing Archaea Blooms in San Francisco Bay. *mSystems* **7**(1): e01270-21. American Society for Microbiology. doi: 10.1128/msystems.01270-21

Raymond PA, Cole JJ. 2001. Gas exchange in rivers and estuaries: Choosing a gas transfer velocity. *Estuaries and Coasts* **24**(2): 312. doi: 10.2307/1352954

Reeburgh W. 2007. Oceanic methane biogeochemistry. *American Chemical Society* **107**(2): 486–513. doi: 10.1021/cr050362v

Repeta DJ, Ferrón S, Sosa OA, Johnson CG, Repeta LD, Acker M, Delong EF, Karl DM. 2016. Marine methane paradox explained by bacterial degradation of dissolved organic matter. *Nature Geosci* **9**(12): 884–887. doi: 10.1038/ngeo2837

Reuer M, Barnett B, Bender M, Falkowski P, Hendricks M. 2007. New estimates of Southern Ocean biological production rates from O2/Ar ratios and the triple isotope composition of O2. *Deep Sea Research Part I: Oceanographic Research* **54**: 951–974.

Robinson AD, Nedwell DB, Harrison RM, Ogilvie BG. 1998. Hypernutrified estuaries as sources of N 2 O emission to the atmosphere: the estuary of the River Colne, Essex, UK. *Marine Ecology Progress Series* **164**: 59–71.

Römer M, Riedel M, Scherwath M, Heesemann M, Spence GD. 2016 Sept 29. Tidally controlled gas bubble emissions: A comprehensive study using long-term monitoring data from the NEPTUNE cabled observatory offshore Vancouver Island. *Geochem Geophys Geosyst*: 1–18. doi: 10.1002/2016GC006528

Rosentreter JA, Borges AV, Deemer BR, Holgerson MA, Liu S, Song C, Melack J, Raymond PA, Duarte CM, Allen GH, et al. 2021. Half of global methane emissions come from highly variable aquatic ecosystem sources. *Nat Geosci* **14**(4): 225–230. Nature Publishing Group. doi: 10.1038/s41561-021-00715-2

Saunois M, Martinez A, Poulter B, Zhang Z, Raymond PA, Regnier P, Canadell JG, Jackson RB, Patra PK, Bousquet P, et al. 2025. Global Methane Budget 2000–2020. *Earth System Science Data* **17**(5): 1873–1958. Copernicus GmbH. doi: 10.5194/essd-17-1873-2025

Schuler KH, Tortell PD. 2023. Impacts of vertical mixing and ice-melt on N2O and CH4 concentrations in the Canadian Arctic Ocean. *Continental Shelf Research* **269**: 105124. doi: 10.1016/j.csr.2023.105124

Seitzinger SP, Kroeze C, Styles RV. 2000. Global distribution of N2O emissions from aquatic systems: natural emissions and anthropogenic effects. *Chemosphere: Global Change Science* **2**: 267–279. doi: 10.1016/S1465-9972(00)00015-5

Smith JM, Chavez FP, Francis CA. 2014. Ammonium Uptake by Phytoplankton Regulates Nitrification in the Sunlit Ocean. Lovejoy C, editor. *PLoS ONE* **9**(9): e108173. doi: 10.1371/journal.pone.0108173

Tang KW, McGinnis DF, Frindte K, Brüchert V, Grossart H-P. 2014. Paradox reconsidered: Methane oversaturation in well-oxygenated lake waters. *Limnology and Oceanography* **59**(1): 275–284. doi: 10.4319/lo.2014.59.1.0275

Tang W, Da F, Tracey JC, Intrator N, Kunes MA, Lee JA, Wan XS, Jayakumar A, Friedrichs MAM, Ward BB. 2024. Nutrient management offsets the effect of deoxygenation and warming on nitrous oxide emissions in a large US estuary. *Sci Adv* **10**(51): eadq5014. doi: 10.1126/sciadv.adq5014

Tang W, Talbott J, Jones T, Ward BB. 2024. Variable contribution of wastewater treatment plant effluents to downstream nitrous oxide concentrations and emissions. *Biogeosciences* **21**(14): 3239–3250. Copernicus GmbH. doi: 10.5194/bg-21-3239-2024

Teeter L, Hamme RC, Ianson D, Bianucci L. 2018. Accurate Estimation of Net Community Production From O_2/Ar Measurements. *Global Biogeochemical Cycles* **32**(8): 1163–1181. doi: 10.1029/2017GB005874

Thierry V, Bittig H, Gilbert D, Kobayashi T, Kanako S, Schmid C. 2025. *Processing Argo Oxygen Data at the DAC Level*. Ifremer. doi: 10.13155/39795

Tian H, Pan N, Thompson RL, Canadell JG, Suntharalingam P, Regnier P, Davidson EA, Prather M, Ciais P, Muntean M, et al. 2024. Global nitrous oxide budget (1980–2020). *Earth System Science Data* **16**(6): 2543–2604. Copernicus GmbH. doi: 10.5194/essd-16-2543-2024

Townsend-Small A, Prokopenko MG, Berelson WM. 2014. Nitrous oxide cycling in the water column and sediments of the oxygen minimum zone, eastern subtropical North Pacific, Southern California, and Northern Mexico (23°N–34°N). *Journal of Geophysical Research: Oceans* **119**(5): 3158–3170. doi: 10.1002/2013JC009580

Uhlig C, Loose B. 2017. Using stable isotopes and gas concentrations for independent constraints on microbial methane oxidation at Arctic Ocean temperatures. *Limnol Oceanogr Methods* **15**(8): 737–751. doi: 10.1002/lom3.10199

Upstill-Goddard RC. 2006. Air–sea gas exchange in the coastal zone. *Estuarine, Coastal and Shelf Science* **70**(3): 388–404. doi: 10.1016/j.ecss.2006.05.043

US Department of Commerce NO and AA. 2025. NDBC. NDBC Station Page 44022. Available at https://www.ndbc.noaa.gov/station_page.php?station=44022. Accessed 2025 Oct 4.

Valentine DL. 2011. Emerging Topics in Marine Methane Biogeochemistry. *Annual Review of Marine Science* **3**(1): 147–171. doi: 10.1146/annurev-marine-120709-142734

Vaquer-Sunyer R, Duarte CM. 2008. Thresholds of hypoxia for marine biodiversity. *Proceedings of the National Academy of Science* **105**: 15452–15457.

Varekamp JC, McElroy AE, Mullaney JR, Breslin VT. 2014. Metals, Organic Compounds, and Nutrients in Long Island Sound: Sources, Magnitudes, Trends, and Impacts. In: Latimer JS, Tedesco MA, Swanson RL, Yarish C, Stacey PE, Garza C, editors. *Long Island Sound*. New York, NY: Springer New York. p. 203–283. doi: 10.1007/978-1-4614-6126-5_5

Vaudrey J. 2017. NEW YORK CITY'S IMPACT ON LONG ISLAND SOUND WATER QUALITY TECHNICAL REPORT. Available at https://vaudrey.lab.uconn.edu/wp-content/uploads/sites/1663/2018/07/2017-11-16-Vaudrey-NYC-N.pdf.

Vlahos P, Whitney MM. 2017. Organic carbon patterns and budgets in the Long Island Sound estuary. *Limnology and Oceanography* **62**(S1): S46–S57. doi: 10.1002/lno.10638

Vlahos P, Whitney MM, Menniti C, Mullaney JR, Morrison J, Jia Y. 2020. Nitrogen budgets of the Long Island Sound estuary. *Estuarine, Coastal and Shelf Science* **232**: 106493. doi: 10.1016/j.ecss.2019.106493

Wallace RB. 2020. Coastal Ocean Acidification: Dynamics and Potential to Affect Marine Mollusks. State University of New York at Stony Brook. Available at https://www.proquest.com/dissertations-theses/coastal-ocean-acidification-dynamics-potential/docview/2455530061/se-2?accountid=3783.

Wallace RB, Gobler CJ. 2021. The role of algal blooms and community respiration in controlling the temporal and spatial dynamics of hypoxia and acidification in eutrophic estuaries. *Marine Pollution Bulletin* **172**: 112908. doi: 10.1016/j.marpolbul.2021.112908

Wan XS, Sheng H-X, Dai M, Casciotti KL, Church MJ, Zou W, Liu L, Shen H, Zhou K, Ward BB, et al. 2023. Epipelagic nitrous oxide production offsets carbon sequestration by the biological pump. *Nat Geosci* **16**(1): 29–36. Nature Publishing Group. doi: 10.1038/s41561-022-01090-2

Wan XS, Sheng H-X, Liu L, Shen H, Tang W, Zou W, Xu MN, Zheng Z, Tan E, Chen M, et al. 2023. Particle-associated denitrification is the primary source of N2O in oxic coastal waters. *Nat Commun* **14**(1): 8280. Nature Publishing Group. doi: 10.1038/s41467-023-43997-3

Wanninkhof R. 2014. Relationship between wind speed and gas exchange over the ocean revisited. *Limnology and Oceanography: Methods* **12**(6): 351–362. doi: 10.4319/lom.2014.12.351

Wanninkhof R, Asher WE, Ho DT, Sweeney C, McGillis WR. 2009. Advances in Quantifying Air-Sea Gas Exchange and Environmental Forcing. *Annual Review of Marine Science* **1**(1): 213–244. doi: 10.1146/annurev.marine.010908.163742

Ward BB. 2008. Nitrification in Marine Systems. In: Capone DG, Bronk DA, Molholland MR, Carpenter EJ, editors. *Nitrogen in the Marine Environment*. Elsevier. p. 199–261.

Ward BB, Kilpatrick KA, Novelli PC, Scranton MI. 1987. Methane Oxidation and Methane Fluxes in the Ocean Surface-Layer and Deep Anoxic Waters. *Nature* **327**(6119): 226–229.

Weiss RF, Price BA. 1980. Nitrous oxide solubility in water and seawater. *Marine Chemistry* **8**(4): 347–359. doi: 10.1016/0304-4203(80)90024-9

West WE, Creamer KP, Jones SE. 2016. Productivity and depth regulate lake contributions to atmospheric methane. *Limnology and Oceanography* **61**(S1): S51–S61. doi: 10.1002/lno.10247

Whitney MM, Vlahos P. 2021. Reducing Hypoxia in an Urban Estuary Despite Climate Warming. *Environ Sci Technol* **55**(2): 941–951. American Chemical Society. doi: 10.1021/acs.est.0c03964

Wiesenburg DA, Guinasso NL. 1979. Equilibrium solubilities of methane, carbon monoxide, and hydrogen in water and sea water. *Journal of Chemical & Engineering Data* **24**(4): 356–360. doi: 10.1021/je60083a006

de Wilde HPJ, de Bie MJM. 2000. Nitrous oxide in the Schelde estuary: production by nitrification and emission to the atmosphere. *Marine Chemistry* **69**(3–4): 203–216. doi: 10.1016/S0304-4203(99)00106-1

Wilke CR, Chang P. 1955. Correlation of diffusion coefficients in dilute solutions. *AIChE Journal* **1**(2): 264–270. doi: 10.1002/aic.690010222

Wilson RE, Swanson RL, Crowley HA. 2008. Perspectives on long-term variations in hypoxic conditions in western Long Island Sound. *Journal of Geophysical Research: Oceans* **113**(C12). doi: 10.1029/2007JC004693

Wilson ST, Bange HW, Arévalo-Martínez DL, Barnes J, Borges AV, Brown I, Bullister JL, Burgos M, Capelle DW, Casso M, et al. 2018. An intercomparison of oceanic methane and nitrous oxide measurements. *Biogeosciences* **15**(19): 5891–5907. doi: 10.5194/bg-15-5891-2018

Wrage N, Velthof G, Van Beusichem M. 2001 Jan 1. Role of nitrifier denitrification in the production of nitrous oxide. *Soil Biology and …*, in press. Available at http://linkinghub.elsevier.com/retrieve/pii/S0038071701000967.

Yin H, Wang Y, Huang J. 2021. Photodegradation-induced biological degradation of treated wastewater effluent organic matter in receiving waters. *Water Research* **204**: 117567. doi: 10.1016/j.watres.2021.117567

Young C, Martin JB, Hanson GN. 2016. Controls on Nitrous Oxide Production in, and Fluxes from a Coastal Aquifer in Long Island, NY, USA. *Journal of Marine Science and Engineering* **4**(4): 71. Multidisciplinary Digital Publishing Institute. doi: 10.3390/jmse4040071

Yu C, He Q, Nie W-B, Zhang T, Wu H, Yang Y, Fu S, Tan X, Chen Y. 2025. Effluent organic matter facilitates anaerobic methane oxidation coupled with nitrous oxide reduction in river sediments. *Water Research* **278**: 123415. doi: 10.1016/j.watres.2025.123415

Zakem EJ, Follows MJ. 2017. A theoretical basis for a nanomolar critical oxygen concentration. *Limnology and Oceanography* **62**(2): 795–805. doi: 10.1002/lno.10461

Zakem EJ, Mahadevan A, Lauderdale JM, Follows MJ. 2020. Stable aerobic and anaerobic coexistence in anoxic marine zones. *ISME J* **14**(1): 288–301. doi: 10.1038/s41396-019-0523-8

Zhan L, Zhang J, Ouyang Z, Lei R, Xu S, Qi D, Gao Z, Sun H, Li Y, Wu M, et al. 2021. High-resolution distribution pattern of surface water nitrous oxide along a cruise track from the Okhotsk Sea to the western Arctic Ocean. *Limnology and Oceanography* **66**: S401–S410. doi: https://doi.org/10.1002/lno.11604

Zheng X, Mei B, Wang Yinghong, Xie B, Wang Yuesi, Dong H, Xu H, Chen G, Cai Z, Yue J, et al. 2008. Quantification of N2O fluxes from soil–plant systems may be biased by the applied gas chromatograph methodology. *Plant Soil* **311**(1): 211–234. doi: 10.1007/s11104-008-9673-6

Zheng Y, Wu S, Xiao S, Yu K, Fang X, Xia L, Wang J, Liu S, Freeman C, Zou J. 2022. Global methane and nitrous oxide emissions from inland waters and estuaries. *Global Change Biology* **28**(15): 4713–4725. doi: 10.1111/gcb.16233